TIDAL TURBINE ROTOR SPACING INFLUENCE ON POWER PERFORMANCE: SIMULATING A SCALED DUAL-ROTOR AXIAL FLOW TURBINE

A Thesis

SUBMITTED TO THE FACULTY OF THE

UNIVERSITY OF MINNESOTA

BY

Javier Felipe Guzman de la Rosa

IN PARTIAL FULFILLMENT OF THE REQUIREMENTS

FOR THE DEGREE OF

MASTER OF SCIENCE

IN MECHANICAL ENGINEERING

Dr. Craig Hill

2023

Acknowledgements

I would like to express my sincere gratitude to my advisor, Dr. Hill, for his guidance, support and encouragement throughout my thesis project. I appreciate his valuable feedback, constructive criticism and insightful suggestions that helped me improve the quality of my work. I would also like to thank my committee members Dr. Mirgolbabaei and Dr. Sam Kelly for their valuable feedback and suggestions in the review process. Their expertise in computational fluid dynamics and turbulent flows improved the quality of this work and gave me significant remarks.

I also want to thank my parents, who have always supported me in my academic pursuits and encouraged me to follow my dreams. They have been my pillars of strength and motivation. I am grateful for their love, care and sacrifice.

I owe a lot to my brothers, who have been my best friends and companions. They have cheered me up, listened to me and shared their experiences with me. They have made my journey more enjoyable and memorable.

Finally, I want to thank my friends, who have been there for me through thick and thin. They have helped me with my research and offered me useful advice. They have also been a source of fun and laughter.

I would like to acknowledge the Minnesota Supercomputing Institute (MSI) for providing me with access to their supercomputers, which were essential in performing the simulations required for this research.

Dedications

To my mom Monica de la Rosa, my dad Gerardo Guzman and my brothers Jose Guzman and Gerardo Guzman.

Thank you for your unwavering support and encouragement throughout my academic journey. Your love and guidance have been the driving force behind my success. I am grateful for the sacrifices you have made to ensure that I had the opportunity to pursue my dreams.

I hope that this achievement brings you as much joy as it brings me. This work is a testament to your unwavering faith in me and your belief in my abilities.

Abstract

Power performance and turbulent wake characteristics of a scaled current-driven marine turbine were simulated using unsteady 3D RANS with the $k-\omega$ SST turbulence model and sliding mesh technique. The turbine is an axial flow, dual rotor tidal turbine with counter-rotating rotors, each with two blades and a diameter of d_T = 0.5 m, representing an approximately 1:40 scale system based on the U.S. Department of Energy's Reference Model 1 (RM1) tidal turbine. Validation of numerical results for three tip speed ratios was performed by comparison with experimental data. The influence of rotor cross-stream spacing on power production was also studied by modeling three distinct lateral rotor separations, equal to $1.2d_T$, $1.4d_T$, and $1.6d_T$. Numerical results showed a good correlation ranging within $\pm 3.8\%$ of turbine performance to experimental measurements for all tip-speed ratios studied, validating the numerical results for power estimation and demonstrating the advantages of this model when dealing with high-flow detachment. Inflow dynamics were captured well, exhibiting a difference of less than 5% compared to experimental data. However, wake dynamics showed a significant difference between numerical results and experimental data, ranging from 16% error at approximately $X/d_T = 4$, up to 170% error at $X/d_T = 8$. Finally, numerical results indicated a tendency for higher power production as the rotors are spaced farther apart, with the resulting power coefficient values of C_p = 0.449, 0.461, and 0483 for lateral rotor spacings of $1.2d_T$, $1.4d_T$, and $1.6d_T$, respectively. This behavior was accredited to the reduction of the flow through the swept area of the rotors, causing what is known as 'choking effect'.

Table of Contents

List of Tables

List of Figures

1. Introduction and Background

In recent years, the impacts generated by using fossil fuels have increased. Clear examples of these impacts are found in environmental problems, health problems, and climate change. Land degradation, water pollution and gas emissions are specific examples of environmental problems. On the other hand, when fossil fuels such as coal, oil and gas are burned, large quantities of pollutants are emitted into the air which lead to people breathing them. Exposure to these emissions can increase the incidence of diseases such as ischemic heart disease (IHD), cerebrovascular disease, chronic obstructive pulmonary disease, and lung cancer [1]. Finally, there is climate change, which is considered a natural process where the planet's temperature, water sources, and winds, among other phenomena, change over time. However, climate changes resulting from global warming has been developing faster, mostly attributed to greenhouse gas emissions from burning fossil fuels. Gases like carbon dioxide and methane are considered greenhouse gases, which function as thermal insulation for the planet, increasing its temperature over time. Because the planet is a system, this increase in temperature is reflected in various areas causing extreme droughts, massive fires, floods, melting of the poles, and rising sea levels, among others. [2].

These negative impacts are directly proportional to the global demand for energy, which has been increasing over the years. According to the 2022 Global Status Report, the global energy demand increased by 4% in 2021, which was primarily covered with coal and natural gas, leading to record carbon dioxide emissions [3]. However, according to Renewables 2021, it is estimated that energy capacity from renewable sources will grow

by approximately 60% between 2020 and 2026, which could cover the continuous increase in coming years. [4]. This sustainable and extractable energy production can come from solar, wind, biomass, geothermal, oceanic and hydraulic sources [5, 6, 7]. From these renewable energy sources, energy from the oceans, generally referred to as marine renewable energy (MRE), is considered a promising alternative that can meet the demand to a large extent in regions with high ocean areas or to a small extent, in regions that have limited resource availability [8].

The Powering the Blue Economy (PBE) initiatives, led by the US Department of Energy's (DOE) Water Power Technologies Office, is an initiative that seeks to protect, understand, and harness the vast energy potential of oceans and rivers. By understanding energy requirements of coastal and maritime markets, the PBE emphasis seeks to advance technologies that take advantage of marine energy to supply these areas and allow greater sustainable growth. In April 2019, the PBE report was released, highlighting potential markets that could benefit from integrating with MRE technologies. Each market was evaluated using multiple analyses, such as the opportunity summary; description of the application and power requirements; description of the market, energy options and geographic relevance; marine energy potential value proposition; and the way forward, including research and development needs and potential partners. Their main conclusion was that there are more potential markets than expected, both for offshore energy and for resilient coastal communities. [9].

Estimates show that in the United States, marine energy technologies could supply approximately 2300 TWh/year, equivalent to the energy demand of 220 million homes and

57% of the energy generated by the US in 2019. It should be noted that this value was estimated with areas considered to be of great generation where amounts of energy of the order of MW or higher could be extracted [10]. For this reason, this value would be even higher if the areas where the amount of capturable energy is of smaller scale (e.g., the Great Lakes of North America) and that were determined as key for different markets in the Powering the Blue Economy Project, are taken into account.

MRE can include offshore wind, offshore solar, and ocean renewable energy (ORE). ORE can be harvested from different sources such as waves, tides, currents and temperature and salinity gradients, among others [11]. However, the technologies to extract this type of energy are still rapidly developing, which requires significant research and development (R&D) to make them competitive with other types of energy generation technologies on a commercial scale. For this reason, the US launched the Reference Model (RM) project as an initiative for R&D of marine energy extraction technologies, proposing and analyzing technically and economically, six different models (RM 1-6) of open-source MRE technologies. The open-source nature of this project seeks to encourage R&D into MRE devices by university researchers and commercial technology developers. The six proposed RMs were designed and based on a reference marine resource site modeled after an actual site in the United States and includes: current energy converters (CEC) encompassing RM1, RM2 and RM4, and wave energy converters (WEC) containing RM3, RM5 and RM6.

The investigation and characterization of these devices is relatively complex and expensive when carried out experimentally, since advanced data collection equipment,

large facilities and their manufacturing are required, among other aspects and limitations. As a solution, R&D leveraging rapid development of computational resources and capabilities enable use of computational fluid dynamics (CFD) to analyze and solve problems involving complex fluid flows around highly complex and technical geometries in a relatively inexpensive way.

In recent studies, CFD has been used to estimate power extraction and characterize the wake, while also investigating phenomena that influence these. One well studied variable is known as the blockage effect, i.e., the ratio of the frontal swept area of the turbine to the cross-sectional area of the channel. Multiple works have used CFD to study blockage effect on the power extracted in both axial flow [12] as cross flow [13] turbines. Results suggest a directly proportional relationship between blockage and MRE turbine power extracted, due to an increase in flow velocity that passes through the turbine rotor(s) when blockage is greater. On the other hand, the authors concluded that there is also faster flow recovery when blocking ratios are high compared to lower blockage ratio environments. This trend is explained by the increase in velocity through and around the turbines when blockage is higher, which increases energy transfer between near and far wake velocity differences. Studies using CFD also illustrate how results from higher blockage, confined turbines can be used to estimate various parameters for unconfined MRE turbines such as drag ratios, power performance, and tip-speed ratios (TSR) [14]. Besides the extensive work done using CFD, multiple authors have also experimentally studied the blockage effect on variables like the power coefficient. A clear example is the work performed by Ross and Polagye (2020), where authors tested a cross-flow and a axial-flow turbine with varying

blockage while keeping non-dimensional parameters, such as free-stream Reynolds and Froude numbers, approximately constant. Authors found that increasing blockage improved turbine performance over a larger range of TSR [15].

Many authors have also used CFD to characterize the performance of different marine turbines. One example is the work by Pacot et al. (2019), where authors used CFD in ANSYS CFX to establish the performance characteristic of their horizontal hydrokinetic turbine built in Switzerland with a designed electrical power output of 1 kW. Authors performed numerical simulations for TSR ranging from λ = 1 to 4.5 and found that the optimal TSR for their specific turbine design corresponded to λ = 2.54 [16]. Another example is the work by Riglin et al. (2016), where authors designed and built a preliminary hydrokinetic turbine prototype for river applications through performance characterization achieved using CFD. Authors performed simulations for five different TSR ranging from λ = 2 to 3.5, finding that the peak mechanical power coefficient of approximately C_p = 0.5 was achieved at a TSR of λ = 2.5 [17].

Other studies have focused on wake recovery and wake interaction, as it is of paramount importance when placing arrays of turbines to increase power production towards farm-scale levels. For example, Ren et al. (2021) performed a CFD investigation of the relationship between water depth where an axial flow turbine is installed and the turbulent wake recovery distance. The authors concluded that deeper placement of the turbine resulted in faster wake recovery, which was explained by the pressure change and increased rate of momentum transfer of the fluid at that depth [18]. Similar results were found by Benavides-Moran et al. (2022), where authors found a slow wake recovery at

shallow rotor immersion due to the free-surface proximity, which also reduced the power extraction. The study was carried out with the volume of fluid (VOF) model implemented in a commercial CFD software ANSYS-Fluent, enabling the capability to model two-phase flows to capture free-surface dynamics in open-channel flow [19].

Until now, few CFD studies have focused on the US DOE RM1 full geometry to fully characterize the wake and analyze geometric modifications to understand implications for power production and/or wake recovery. Javaherchi et al. (2014, 2017) conducted numerical studies to investigate the effect of TSR variation (λ = 5.5 to 10.3) on the performance and wake structure associated with an RM1 laboratory-scale model turbine, using two different numerical approaches: the Rotating Reference Frame (RRF) model and the Blade Element Model (BEM). The authors concluded that the RRF model showed limitations to model the effect of dynamic stall on power coefficients at low TSRs and of solid walls in the wake recovery. On the other hand, the authors noted that the BEM model showed limitations to model turbine performance at very low and high TSRs, under-predicting the performance due to lacking to ability to appropriately model dynamic stall and 3D centrifugal flow. However, it is important to highlight that in this study only one rotor was considered, ignoring the interaction between both rotors, the RM1 central support tower, and their wakes [20, 21].

To date, the only full geometry scaled RM1 studies published were performed by Niebuhr et al. (2022), where the authors used experimental results obtained for a 1:40 scaled version of this turbine as a validation case for their numerical model similar to the studied completed in this report. The authors executed CFD simulations to estimate the

power coefficient for the optimum TSR, evaluate multiple turbulence models, the effect of boundary conditions selection and different rotor modeling techniques. All simulations were conducted using the commercial modeling software Siemens STAR-CCM+ [22]. However, the authors did not propose or analyze any geometric modifications to affect the wake recovery or power output.

On the contrary, an example of an experimental study performed on a scaled version of the full RM1 assembly is the published work done by Hill et al. (2020) where a 1:40 scaled version of the dual-rotor axial-flow turbine was characterized for a variety of TSRs in an open-channel flume. Flow environment was characterized using acoustic Doppler velocimeters, whereas the turbine performance was characterized using torque sensors and speed control. Also, velocity measurements were recorded in the inflow up to -5 rotor's diameter upstream and in the wake flow field up to 24 rotor's diameters downstream. Some key findings were that maximum performance of $C_p = 0.48$ occurs near a $\lambda \approx 5.1$ and elevated levels of turbulent kinetic energy in the near wake attributed mostly to the instabilities induced by the center supporting tower [23]. Other studies correspond to the work done by Lust et al. (2020) where authors used particle image velocimetry (PIV) to measure velocity up to two diameters downstream of the rotor plane in a single rotor 1:25 scaled version of the RM1. The authors described in detail the flow field presented in the near wake of the turbine in the presence of surface gravity waves [24].

In this thesis, a numerical study was performed and validated against experimental [23] and numerical data [22]. The turbine studied consisted of a 1:40 geometric scaled model

of the DOE RM1 turbine, which is a dual-rotor axial flow turbine with counter-rotating rotors, each with a diameter $d_T = 0.5\ m$.

2. Methodology

In fluid mechanics, the movement of fluid can be described by the Navier-Stokes equations, which is a system of second-order nonlinear partial differential equations. Limited analytical solutions are known for this system of equations, except for very specific cases where simplifications and assumptions are made about the fluid, flow, or geometry. Typical assumptions include laminar, incompressible, steady, 2D flow, such as when the flow is between two parallel plates. When the velocity of the fluid is relatively low, the flow is known as laminar with a Reynolds number (Re) below Re = 2300 and analytical and numerical solutions are easily found. However, when the flow has a high velocity (Re>4000), the flow is said to be turbulent, and the solution of the Navier-Stokes equations is complicated. For this reason, the solution is usually obtained by using numerical methods applying corresponding boundary conditions and assumptions for each specific case. The Navier-Stokes system of equations for a Newtonian incompressible fluid is represented by the conservation of mass (1) and conservation of momentum (2):

$$\frac{\partial U_i}{\partial x_i} = 0 \tag{1}$$

$$\frac{\partial U_i}{\partial t} + \frac{\partial U_i U_j}{\partial x_j} = -\frac{1}{\rho}\frac{\partial p}{\partial x_i} + \frac{\mu}{\rho}\frac{\partial^2 U_j}{\partial {x_j}^2} + f_i \tag{2}$$

where U, p, ρ and μ are velocity, pressure, fluid density, and dynamic viscosity, respectively. Body forces and external forces applied to the fluid are represented by the term f_i. The subscripts indicate the Cartesian coordinate direction being applied to the

variable, where *i* and *j* can take on values of 1, 2, or 3 corresponding to the x, y, or z-directions, respectively.

Due to the fact that pressure and velocity change randomly in time and position, Osborne Reynolds proposed the idea of decomposing these instantaneous quantities, or exact solutions, (φ) in their time-average ($\bar{\varphi}$) and fluctuating components (φ') (3).

$$\varphi = \bar{\varphi} + \varphi' \tag{3}$$

This technique is known as Reynolds decomposition and applying this to (1) and (2), the new equations for conservation of mass (4) and momentum (5), known as the Reynolds-averaged Navier-Stokes equations (RANS).

$$\frac{\partial \bar{U}_i}{\partial x_i} = 0 \tag{4}$$

$$\frac{\partial \bar{U}_i}{\partial t} + \frac{\partial \bar{U}_i \bar{U}_j}{\partial x_j} = -\frac{1}{\rho}\frac{\partial \bar{U}}{\partial x_i} - \frac{\mu}{\rho}\frac{\partial^2 \bar{U}_i}{\partial {x_j}^2} - \frac{\partial \overline{U'_\iota U'_J}}{\partial x_j} + f_i \tag{5}$$

An additional term appears in (5), that includes the term $\overline{U'_\iota U'_J}$, which is known as the Reynolds stress tensor. In three-dimensional scenarios, this Reynolds stress tensor is a 3 by 3 matrix. Additional equations must be used in order to model this tensor to fully close (5), giving way to turbulence models in trying to predict or model a term known as kinetic eddy viscosity or turbulent viscosity (υ_t).

2.1. Turbulence Models

Multiple turbulence models have been developed to model turbulence. Widely used models consist of the Spalart-Allmaras model, turbulence kinetic energy (k) and dissipation rate (ε) model (i.e., the $k-\varepsilon$ model), k and specific dissipation rate (ω) model

(i.e., the $k-\omega$ model), Transition SST model, Reynold stress model (RSM) model, Detached Eddy Simulation (DES) and Large Eddy Simulation (LES) model, among others. The following sections provide brief overviews of some key characteristics of each, following by a description of techniques primarily used in modeling rotating turbine geometries.

2.1.1. Spalart-Allmaras Model

The Spalart-Allmaras (S-A) model is a one-equation model derived using dimensional analysis that uses a modeled transport equation for the turbulent viscosity (ν_t) [25]. This model was created specifically for aerospace applications involving wall-bounded flows and then adopted for incompressible flow calculations. The S-A model and has been shown to give good results compared to experimental data [26], more specifically for problems with boundary layers subjected to adverse pressure gradients.

2.1.2. k-ε Model

Two equations models such as $k-\varepsilon$ and $k-\omega$, allow the determination of a turbulent length and time scale by solving two additional equations. In the case of the $k-\varepsilon$ model, proposed by Laundes and Spalding [27], two equations are solved for the turbulent kinetic energy (k) and its dissipation rate (ε). The equation for k is derived from the exact equation, while ε was obtained using physical reasoning. This model assumes that the flow is completely turbulent, neglecting the effects of molecular viscosity. Over the years, many modifications have been proposed to improve this model, becoming known as the renormalization group (RNG) $k-\varepsilon$ model and the realizable $k-\varepsilon$ model, among others.

Once k and ε are calculated, the turbulent viscosity is computed by relating these two quantities by (6).

$$\nu_t = \rho C_\mu \frac{k^2}{\varepsilon} \tag{6}$$

where C_μ is a constant determined experimentally.

Although the $k - \varepsilon$ model performs well in predicting the mean velocity fields in wall-bounded shear flows and is frequently used due to the fact that this model has proven insensitivity to freestream values, it has its own difficulties and limitations in viscous sublayer formulation and boundary layers in adverse pressure gradients [28].

2.1.3. k-ω Model

The additional widely used two-equation model is the $k - \omega$ model, introduced by Wilcox [29] in 1998, containing two added equations, one for k (7) and its specific dissipation rate, ω (8). This model aims to model the near-wall interactions more accurately than the $k - \varepsilon$ model, making it a suitable candidate for resolving internal flows, separated flows, and internal flows through curved geometries. As this model has been modified over the years, additional terms have been added to both equations with the aim of improving the accuracy of the model for predicting free shear flows.

$$\frac{\partial}{\partial t}(\rho k) + \frac{\partial}{\partial x_i}(\rho k U_i) = \frac{\partial}{\partial x_j}\left(\Gamma_k \frac{\partial k}{\partial x_j}\right) + G_k - Y_k + S_k + G_b \tag{7}$$

$$\frac{\partial}{\partial t}(\rho\omega) + \frac{\partial}{\partial x_i}(\rho\omega U_i) = \frac{\partial}{\partial x_j}\left(\Gamma_\omega \frac{\partial \omega}{\partial x_j}\right) + G_\omega - Y_\omega + S_\omega + G_{\omega b} \quad (8)$$

where G_k represents the generation of turbulence kinetic energy due to mean velocity gradients, G_ω represents the generation of ω, Γ_k and Γ_ω represents the effective diffusivity of k and ω due to turbulence, G_b and G_ω accounts for buoyancy terms and S_ω and S_k are user-defined sources terms [30].

After solving k and ω, the turbulent viscosity is calculated using (9).

$$\nu_t = \alpha^* \frac{\rho k}{\omega} \quad (9)$$

where α^* is a coefficient that damps the turbulent viscosity causing a low-Reynolds number correction.

However, the $k-\omega$ model also has some disadvantages. One of the main disadvantages is its sensitivity to freestream turbulence intensity values, which can lead to inaccurate flow field predictions. Another disadvantage is the inability of the $k-\omega$ model to accurately predict highly anisotropic flows, such as flows over highly swept wings or flows with significant crossflow, whereas other models such as the Reynolds Stress Model (RSM) are preferred. To address some of these issues, Wilcox [31] in 2008 proposed the incorporation of two modifications to the model: the addition of a cross-diffusion term and a built-in stress-limiter modification. The addition of the cross diffusion to the ω term improved the prediction of some free shear flows and significantly reduced the model's sensitivity to the freestream boundary conditions on turbulence parameters. On the other

hand, the inclusion of the stress limiter allowed the model to predict with good agreement properties of shock-separated flows for flows from transonic to hypersonic regimes.

2.1.4. k-ω SST Model

Despite the efforts of various authors to eliminate the effects of freestream dependency of the $k-\omega$ model, this objective has not yet been achieved and a more detailed discussion can be found in [28]. Attempting to improve the $k-\omega$ and the $k-\varepsilon$ models, Menter [32] proposed another turbulence model which he named as the Shear Stress Transport (SST) $k-\omega$ turbulence model. The SST $k-\omega$ was developed by retaining the robust and accurate formulation of the $k-\omega$ model in the near wall region while taking advantage of the freestream independence of the $k-\varepsilon$ model in the outer part of the boundary layer. To accomplish this, the $k-\varepsilon$ model is transformed into a $k-\omega$ formulation and through a blending function each model is used in its appropriate region, meaning that the blending function will gradually increase from zero in the wake and in free shear layers, activating the $k-\varepsilon$ model, to one in the near wall region, activating the $k-\omega$ model.

The second improvement that the SST $k-\omega$ has is the inclusion of the important effect of the transport of the principal turbulent shear stress (τ) and therefore on μ_t. By including the effects of τ, results have been found to improve when dealing with adverse pressure gradient flows. In this new model, μ_t is calculated using (10) [30].

$$\nu_t = \frac{\rho k}{\omega} \frac{1}{max\left[\frac{1}{\alpha^*}, \frac{SF_2}{\alpha_1 \omega}\right]} \tag{10}$$

where S is the strain rate magnitude and F_2 is given by (11).

$$F_2 = \tanh\left(\phi_2{}^2\right) \tag{11}$$

where $\phi = max\left[2\frac{\sqrt{k}}{0.09\omega y}, \frac{500\mu}{\rho y^2 \omega}\right]$ and y is the distance to the next surface. All other model constants have the same value as for the $k-\omega$ model.

2.1.5. Large Eddy Simulation (LES) Model

Turbulence can be caused by factors like obstruction or sharp corners, high velocities that overcome viscous forces, and low-pressure regions, among others. Friction between adjacent layers of fluids and their surroundings can form swirls or eddies, which vary in size and shape. However, there are cases where solving some or all eddies are extremely important and RANS turbulence models are discarded, implementing higher-order models such as LES and Direct Numerical Simulation (DNS). When employing LES, large eddies of the flow that depend on the geometry are resolved directly, while smaller eddies are modeled, which are usually less dependent on the geometry and tend to be more isotropic. By solving only a fraction of the eddies present in the flow, one can use much coarser meshes and larger time steps compared to DNS. However, as LES resolves some eddies, it in turn requires a finer mesh and smaller time steps than RANS models, where all eddies are modeled. This, in the end, results in an increase of the computational costs compared to RANS, which in industrial applications, high-performance computing is a necessity. The filtering process for categorizing eddies as 'small' or 'large' can be performed explicitly or implicitly way. In the explicitly filtering, an integral operator with a specified kernel is used and a cutoff length scale or width is set. On the other hand, the implicitly filtering happens by using a cutoff length scale determined by the mesh resolution, where scales in size below the smallest cell in the mesh are modeled and bigger scales are solved [33]. Yet,

most industrial applications include complex geometries, high velocities, or a combination of both, requiring absurd amounts of computational resources. Current technological development has the scope of increasing the processing and storage capability but is still not available to date, reducing the number of cases where LES can be applied in industrial applications.

2.1.6. Direct Numerical Simulation (DNS)

Finally, DNS is a type of simulation where the Navier-Stokes equations are numerically solved without any turbulence model. In other words, every eddy presented in the flow is solved despite the size, from the smallest dissipative scales up to the integral scales associated with the motions containing the most kinetic energy. In order to achieve this, one has to guarantee fine meshes and small time steps that will cover all temporal and spatial scales in the problem. For this reason, the cost required for DNS to solve the entire range of scales has been estimated to be proportional to $Re_t{}^3$, where Re_t is the turbulent Reynolds number [30]. Evidently, for practical engineering problems involving high Reynolds number, the cost becomes prohibitive, and DNS is discarded as an option for simulating the problem.

2.1.7. Turbulence Model in the Present Study

Due to the complexity of the domain, the flow's Reynolds number and the limited time, the $SST\ k-\omega$ model has been chosen for the present work as its able to capture the separated flow near the tip of the blades more accurately and is able to reproduce experimental data in good agreement compared to other two-equation turbulence models [34] requiring reasonable simulation times and computational resources. This model has

been widely used to numerically capture the flow field around hydrofoils for various Reynolds numbers [35, 36], vertical axis wind turbines [34], horizontal axis wind turbines [37], and in many hydrokinetic turbines studies [19, 38, 39].

2.2. Rotor Modeling Techniques

When dealing with rotating or moving domains, multiple techniques have been created to obtain increased accuracy of the flow by modeling the effect of this rotation/translation on the flow or the actual movement of the domain. Typical examples of this type of analysis are rotating blades, impellers, and moving walls, among others. The Actuator Disk (AD) technique is a mathematical approach to approximate the rotor using an infinitely thin source of momentum modeled as a pressure jump across the disk [40]. In other words, the disk represents the forces applied to the surrounding flow field by the actual rotor of the turbine, as a momentum sink term in the computational domain [41]. This technique reduces the computational cost and time as the actual geometry of the rotor does not need to be solved, eliminating the need for fine meshes. This technique has been used by previous authors to accurately numerically capture the fluid-machine interaction and its wake description for applications such as flows around the helicopter main rotors [40], single wind turbine rotors [42] and multiple turbines under different arrangements [43, 44, 45]. However, this technique resembles the Blade Element Momentum (BEM) method in that the aerodynamic forces must be determined from measured airfoil characteristics using a blade-element approach [46], which are not always available for all airfoils, especially when new turbines are designed. Other authors, such as Kang et al. (2014) [47] performed a detailed comparison using the AD technique embedded with LES turbulence model and

found that the method is not sufficient to correctly simulate the development of the turbine's wake and proved that the far wake is sensitive to the stability of the vortical structure in the near wake.

Another widely used technique to model rotating geometries is known as Moving Reference Frames. In this technique, the RANS equations are solved in a single reference frame (SRF) or multiple reference frames (MRF), which allows an unsteady problem in the stationary (inertial) frame to become steady with respect to the moving frames [30]. When the entire domain is studied as one rotating domain, it is known as SRF and is simple to implement. However, SRF is not capable of handling problems that involve multiple rotating parts or stationary components. On the other hand, MRF is used when performing simulations where one or multiple subdomains, enclosing the rotating objects, are studied using moving reference frames, but the rest of the domain is divided into several subdomains and studied in the stationary reference frame. The equations of motion are first solved in each moving reference frame, declaring the appropriate boundary conditions, and then the effects of Coriolis and centrifugal acceleration of the fluid is augmented as body forces in the momentum equations [48]. This technique has been found to be relatively simple, robust, and efficient, reasons for why authors have used this technique to simulate hovering rotors [49], cooling fans [50], wind turbines [51, 52], hydrokinetic [53] and tidal turbines [54], among others. However, in some cases, authors have found that when employing this technique in cases like tidal turbines, it has underestimated the power and thrust of the turbine. Also, low turbulence intensity values were found in the wake of the turbine, which authors attributed to the inability of this technique to resolve the rotation-

induced turbulent intensity, as the domain is placed at a specific position (frozen rotor) [54].

When trying to capture the unsteady effects in turbulent flows and when interactions between rotating and stationary domains are crucial, a widely employed technique called sliding mesh is preferred as it gives more accurate results when compared with experimental data. When using this approach, the computational domain is divided into multiple zones, which can be stationary, moving, or a combination of both. In contrast to MRF, the sliding mesh technique allows the sliding of the mesh relative to other zones along the interfaces between them. This technique requires more computational resources and longer simulations as the cell connectivity needs to be re-established each time that sliding occurs [55]. In Ansys Fluent, a generic transport equation (12) is applied to all model equations such as turbulence, energy, species, phases and so on [30].

$$\frac{d}{dt}\int_V \rho\phi dV + \int_{\partial V} \rho\phi\left(\vec{u} - \overrightarrow{u_g}\right)\cdot d\vec{A} = \int_{\partial V} \Gamma\nabla\phi \cdot d\vec{A} + \int_V S_\phi dV \qquad (12)$$

where $\vec{u}$ is the flow velocity, $\overrightarrow{u_g}$ is the mesh velocity of the moving mesh, Γ is the diffusion coefficient and S_ϕ is the source term of ϕ. Also, ∂V represents the boundary of the control volume V.

It should be stressed that when using the sliding mesh technique, all cells retain their original shape and volume (no deformation occurs) and because the mesh is moving, the solutions to (12) will be inherently unsteady. The connection between the two adjacent zones is coupled by two interfaces, one on each zone, which must be guaranteed to be

identical or minimally different when spatially discretizing these boundaries. Finally, an interpolation of field variables between the adjacent interfaces is performed on the boundary cell faces in every timestep, which should be also guaranteed to be small enough to warrant that the interface slides by no more than half a cell in one timestep [56].

The sliding mesh technique has been extensively used in vessel tanks [57], vertical wind turbines [58, 59] and hydrokinetic turbines [38, 60]. One advantage to using this technique is the ability to predict the wake of turbines, which is important when studying arrays of turbines as the performance of downstream turbines is influenced by the oncoming flow. Silva et al. (2016) performed an unsteady numerical study of wake characteristics in a horizontal-axis hydrokinetic turbine [61], using the sliding mesh technique, and concluded that the numerical results for performance and wake characteristics had good concordance with experimental data. Tabib et al. (2017) compared three rotor modeling techniques: the Actuator Line model (ALM), MRF and the sliding mesh. Authors concluded that the sliding mesh technique had the minimum difference compared to the results found in [62]. However, authors found that the sliding mesh predicted a higher wake deficit in the near wake region and a faster wake recovery compared to the ALM [63]. In more recent studies, Niebuhr et al. (2022) performed numerical modelling of axial hydrokinetic turbine wake in channel flow, comparing different rotor modelling techniques and models. Focusing on the results obtained for the turbine's performance, authors concluded that the results lied within 5% of the experimentally measured results. However, when using the sliding mesh technique coupled with an eddy viscosity turbulence model, authors determined that adequate capture of the

wake was limited and an over-prediction by up to 20% was observed in the near wake and significantly delayed wake recovery. Authors attributed this inaccuracy to the lack of RANS models in resolving small eddies, which can only be fixed by employing higher-order models such as hybrid models or LES [22].

2.3. Computational Domain and Boundary Conditions

The sliding mesh technique coupled with the $k-\omega$ SST turbulence model were used to simulate the flow field associated with the 1:40 scale model of the US DOE RM1. All variables for the $k-\omega$ SST turbulence model were kept as the default values. ANSYS Fluent version 2022 R2 running on supercomputers available at the Minnesota Supercomputing Institute (MSI) was used. The RM1 is an axial flow tidal turbine with dual counter-rotating rotors, each with a rotor diameter, $d_T = 0.5\,m$. Each rotor and nacelle are mounted on a crossarm assembly which are fixed on a monopile foundation, visualized in Figure 1. The dual rotors are offset by $1.4d_T$ from each rotor centerline, giving an overall width from blade tip to tip of 1.2 m. The rotor centerline is submerged $1d_T$ below the free surface and positioned $1d_T$ above the seabed. The total tower height is $2d_T$, fully submerged in the flow and it is un-tapered. The modeled scale blades for the RM1 used NACA-4415 instead of the original full-scale RM1 design blade profile (NACA-63(4)-24) due to a lower Reynolds number during experiments and the availability of performance coefficients data [23].

Figure 1. Photo of the scaled RM1 dual-rotor physical model in the UMN SAFL Main Channel. Adapted from [64]. The arrow indicates flow direction.

The entire turbine was placed in an open-channel domain that extended -8d_T upstream to 30d_T downstream from the plane of rotation. Each rotor was enclosed in a cylindrical domain where a rotating mesh was created. This cylinder was created using a diameter 10% larger than d_T, improving numerical efficiency and numerical stability. The size of the rotating domain was selected having in consideration previous similar studies [22]. The total depth (2d_T) and width (5.5d_T) of the domain matched the experimental dimensions in [23] (Figure 2). This inlet domain length was selected to allow full flow development before the rotor was reached. This length is particular for each case studied as it depends on many factors such as the turbulence model used, TSR and solidity, among others. It has

been previously found that an incorrect selection of the inlet length affects the performance of the turbine because of an incorrect estimation of velocity magnitude at the turbine and incorrect prediction of the upstream induction field [65, 66].

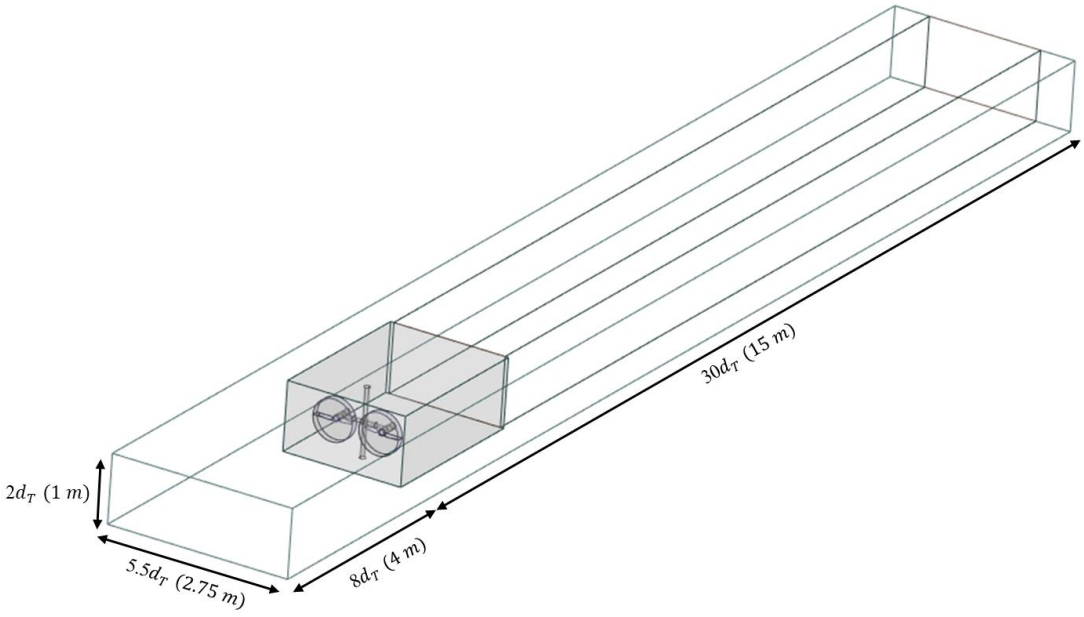

Figure 2. Dimensions of the computational domain, which closely match the experimental conditions. Flow is lower-left to upper-right.

A similar case occurs with the position of the outlet in the computational domain. This boundary condition should be positioned far enough downstream to allow for flow development and guarantee no interference with wake dynamics. When focusing on power characterization of turbines, authors have used an outlet length of up to $15d_T$ and have acquired results with good agreement when compared to experimental data [67, 68, 69]. However, when the aim of the study is to characterize the near and far wake dynamics, a longer domain must be implemented. Previous numerical studies on wind turbines have

used outlet lengths of up to $30d_T$ downstream of the turbine and have obtained satisfactory wake results even in the near wake region [70]. Other authors have implemented the same study to hydrokinetic turbines, using outlet lengths of $30d_T$ and reported good agreement compared to experimental data measured up to a length of $25d_T$ downstream of the turbine [71]. More recent studies performed on hydrokinetic turbines indicated that flow recovery can extend up to $35d_T$ downstream of the turbine [72]. In the present study, a length of $30d_T$ downstream of the plane of rotation was selected in order to not affect the wake dynamics and allow comparison between numerical and experimental data.

Upstream boundary conditions used a constant and uniform velocity and turbulence level at the domain inlet. These values match experimental hub height average values reported in [23] of $U_{in} = 1.04\ m/s$ for velocity in the axial (flow) direction and $I_{in} = 5\%$ for the hub height turbulent intensity. The outlet of the domain was set to a gauge uniform pressure of $P_{oulet} = 0\ Pa$ and a turbulent intensity of $I_{out} = 5\%$. For the top face of the domain where the water-air interface is located, a symmetry boundary condition was set, ignoring the effects from free surface deformation and reducing the computation time. In Ansys Fluent, this condition assumes that the normal velocity at the symmetry plane is zero and the normal gradients of all variables at a symmetry plane is also zero [30]. Finally, for the side and bottom faces of the channel as well as the rotor, nacelle and supporting tower's walls, a no-slip condition was set, assuming that the fluid has zero velocity relative to the boundary and allowing for the development of the boundary layer. All boundary conditions are summarized in Figure 3.

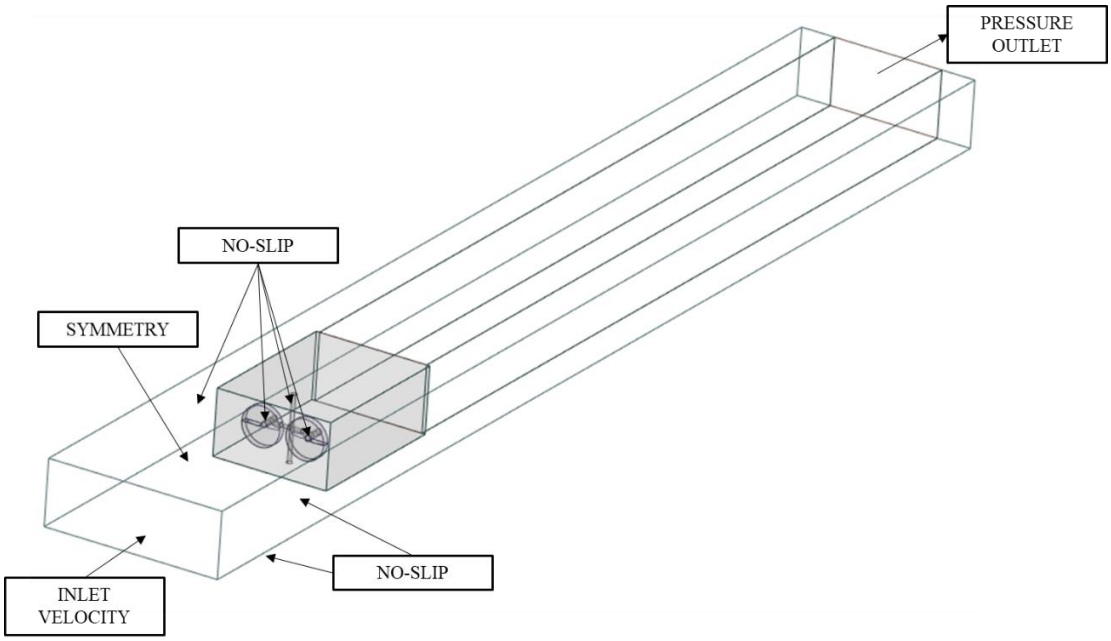

Figure 3. Employed boundary conditions for the computational domain.

Water with a density of $\rho_w = 998.2\ \frac{kg}{m^3}$ and a dynamic viscosity of $\mu_w = 1.003x10^{-3}\ \frac{kg}{m \cdot s}$ was selected as the working fluid. For reference values used in monitors and calculations, the following values were established: a rotor swept area by each rotor of $A_T = 0.1963\ m^2$, a length equal to the rotor's radius $L_T = 0.25\ m$, and a reference velocity equal to the inlet's velocity of $U_{ref} = 1.04\ m/s$. Pressure and velocity were coupled by the Coupled Scheme, which solves the momentum and pressure-based continuity equation together. This technique is known to be used when dealing with complicated domains where the generation of the mesh can be difficult and poor elements are present [30]. Second-order spatial discretization for pressure and momentum and first-order discretization for turbulent kinetic energy and specific dissipation rate were

implemented. On the other hand, first-order implicit was specified as the transient formulation and all other parameters were kept as default by Ansys Fluent.

Regarding the spatial discretization of the computational domain, Ansys Meshing was used to generate all meshes used in this study. The computational domain consists of five different subdomains that facilitated the creation and refinement of the mesh while also the rotation specification. These five subdomains consisted of two rotating subdomains, labeled as left and right rotor, a near wake, a far wake and the full subdomain as seen in Figure 4.

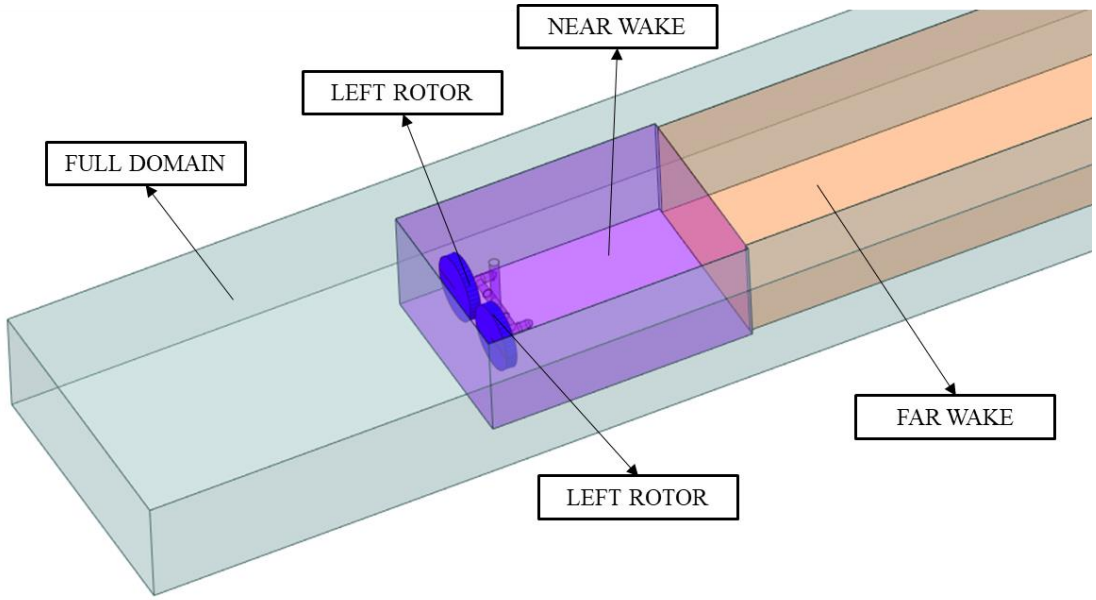

Figure 4. Created subdomains for the computational domain.

Each of the turbine's rotors is embedded in a rotating subdomain, which is separated and connected to the stationary subdomain by a sliding mesh (Figure 5). Similar meshes were guaranteed to be in both faces creating the interface necessary for the sliding mesh, assuring accuracy and stability while performing the transient analysis. A well-refined

mesh was created in the vicinity of the walls in order to capture and achieve an accurate solution of the boundary layer.

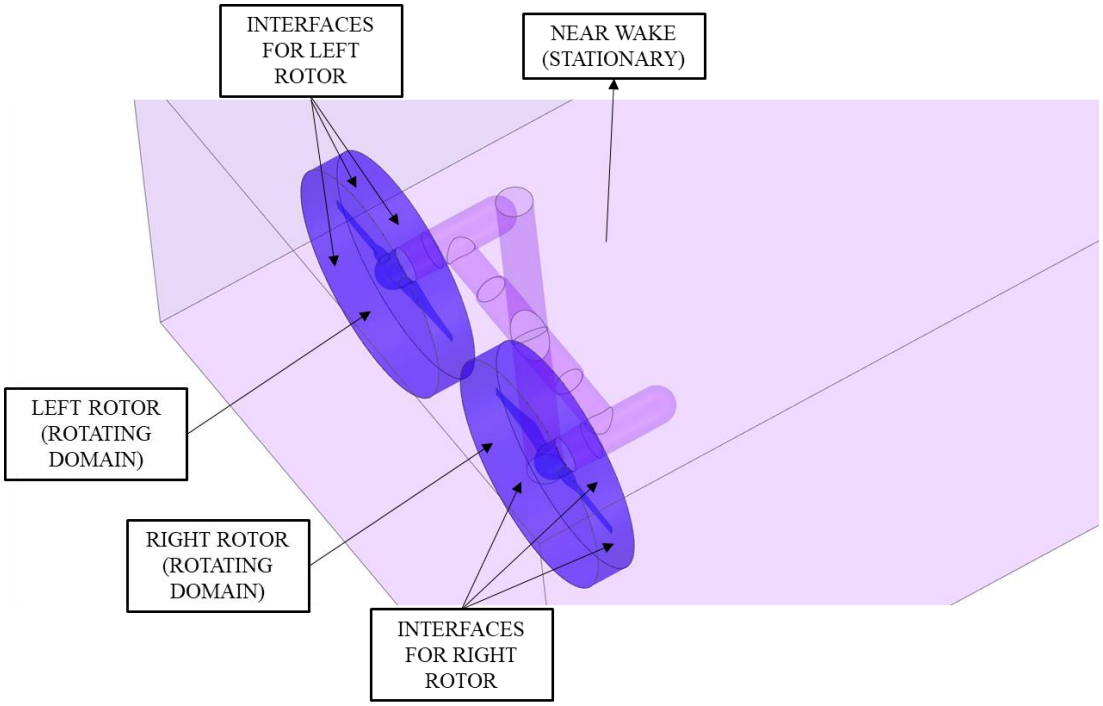

Figure 5. Interfaces utilized for sliding mesh technique in computational domain.

2.4. Turbine performance and wake dynamics characteristics

Multiple nondimensional parameters are used when characterizing a turbine. In this section, a brief explanation of common non-dimensional parameters is provided.

2.4.1. Reynolds Number (Re)

The Reynold number is a nondimensional parameter in fluid dynamics that relates the inertial forces to viscous forces [73]. In hydro turbines this number can be based on either the rotor's diameter (Re_D) or chord length (Re_c) and depends on the kinematic viscosity of

the fluid and a characteristic velocity of the flow. In this work, the chord-based Reynolds number was selected and calculated using (13).

$$Re_c = \frac{U_{rel} \cdot c}{\nu} \tag{13}$$

where the kinematic viscosity is $\nu = \mu/\rho$, c is the mid-span blade chord length, and U_{rel} is the relative velocity. U_{rel} is a function of the free-stream velocity and the tip speed ratio.

When turbines are placed in a bounded flow, the velocity around the turbine increases due to the spatial restriction that the channel's walls and free surface cause. In order to achieve dynamic similarity (i.e., similar hydrodynamic forces) on both scaled and full-scale systems, Reynolds numbers should be kept similar. In the present study, a $Re_c = 3.1x10^5$ was guaranteed to match the Re_c used in the experiments.

2.4.2. Power Coefficient (C_p)

A non-dimensional parameter called the power coefficient C_p is used to quantify the relationship between the rotor mechanical power to the available hydrokinetic power in the approaching flow, giving an idea of the hydrodynamic efficiency of the rotor [74]. Time-averaged turbine mechanical power coefficient $\overline{C_p}$ can be determined using (14) from the time-averaged power ($\overline{P_T}$) and velocity $\overline{U}$, which the later is usually measured 3-5 d_T upstream.

$$\overline{C_p} = \frac{\overline{P_T}}{\frac{1}{2}\rho A_T \overline{U}^3} \tag{14}$$

where A_T is the turbine's flow-facing area or rotor swept area.

In Ansys Fluent, users can monitor the momentum coefficient C_M over a specific surface, which can later be related to the C_p by using the equation $C_p = \lambda \cdot C_M$, where λ is the tip speed ratio (TSR). In Ansys Fluent, the C_M is calculated by (15), using the total moment (M) vector about a specified center of rotation.

$$C_M = \frac{M}{\frac{1}{2}\rho {U_{ref}}^2 A_T L_T} \tag{15}$$

In the present study, U_{ref} was matched to the experimental velocity value at hub height measured $5d_T$ upstream of the turbine in [23] and a value of $L_T = d_T/2$ was set. The total moment vector about a specified center is computed by summing the cross product of the pressure and viscous force vectors on each face with the radial vector from the specified moment center [30].

2.4.3. Tip Speed Ratio (TSR)

The TSR or λ relates three important variables: the turbine's rotational speed, the rotor diameter, and the incoming flow's speed. It is defined as the relationship between the linear turbine blade tip speed and the incoming flow's speed (16).

$$\lambda = \frac{\omega \cdot d_T}{2 \cdot U_{ref}} \tag{16}$$

A turbine with its specific design will operate in a range of variations of λ, but will have maximum efficiency or C_p at optimal λ [75]. In the experiments of [23], the scaled RM1 model was studied for a λ range of 1.5 to 9, where authors found that the best operating point for both rotors occurred at approximately $\lambda = 5.07$.

2.4.4. Velocity Deficit

Placing a turbine inside a moving flow causes a disturbance in the downstream region, triggering strong turbulent mixing and a complex eddy system known as the wake. The flow past the turbine loses kinetic energy, and it takes a finite length to fully recover its velocity. This distance is known as the wake-recovery distance, and it is measured from the turbine location until the flow has recovered 90% of its initial flow velocity [76]. This parameter is crucial when defining the spacing between turbines in an array configuration. In order to determine the wake-recovery distance, a velocity deficit in the wake is measured and calculated using (17).

$$U_{def} = \frac{\left|U_{ref} - U_x\right|}{U_{ref}} \tag{17}$$

where U_{def} is the velocity deficit and U_x is the velocity at position x.

Characterizing the wake of both near-wake ($x/d_T < 5$) and far wake ($x/d_T > 5$) of each turbine placed in an array will aid in improving the performance of the whole system which translates to an increase in overall energy production. For this purpose, when performing experimental characterization, variables such as velocity can be measured using techniques such as Acoustic Doppler Velocimetry (ADV) [77, 78], Laser Doppler Velocimeter (LDV) [79, 80], and Particle Image Velocimetry (PIV) [81, 82]. However, these techniques require expensive equipment and prolonged time to set up and test. For this reason, CFD has become a leading tool to characterize the power performance and wake of turbines [83, 84, 85].

3. Results and Discussion

This section details results obtained from various numerical simulations performed. First, mesh and time step independence studies are discussed for validation of numerical results compared to experimental data. Next, the ability of the $SST\ k-\omega$ turbulence model in handling different types of flows is presented by simulating multiple cases with different TSR, encompassing low and high detachment of flow. Following this, an explanation and comparison between numerical and experimental results of the inflow and wake is presented. Finally, the relationship between rotor spacing and C_p of the RM1 dual-rotor axial flow turbine for three different lateral rotor spacing configurations is discussed.

3.1. Mesh and Time Step Independence Study

The non-dimensional parameter y^+ defined as $y^+ = yu^*/v$, where y is the normal distance from the wall and u^* is the friction velocity, was monitored and limited to 1 across the rotors, nacelles and supporting arms and tower, as presented in Figure 6. This limitation is recommended when using this model and ensures that the viscous sub-layer (in the region $y^+ < 5$), is fully resolved.

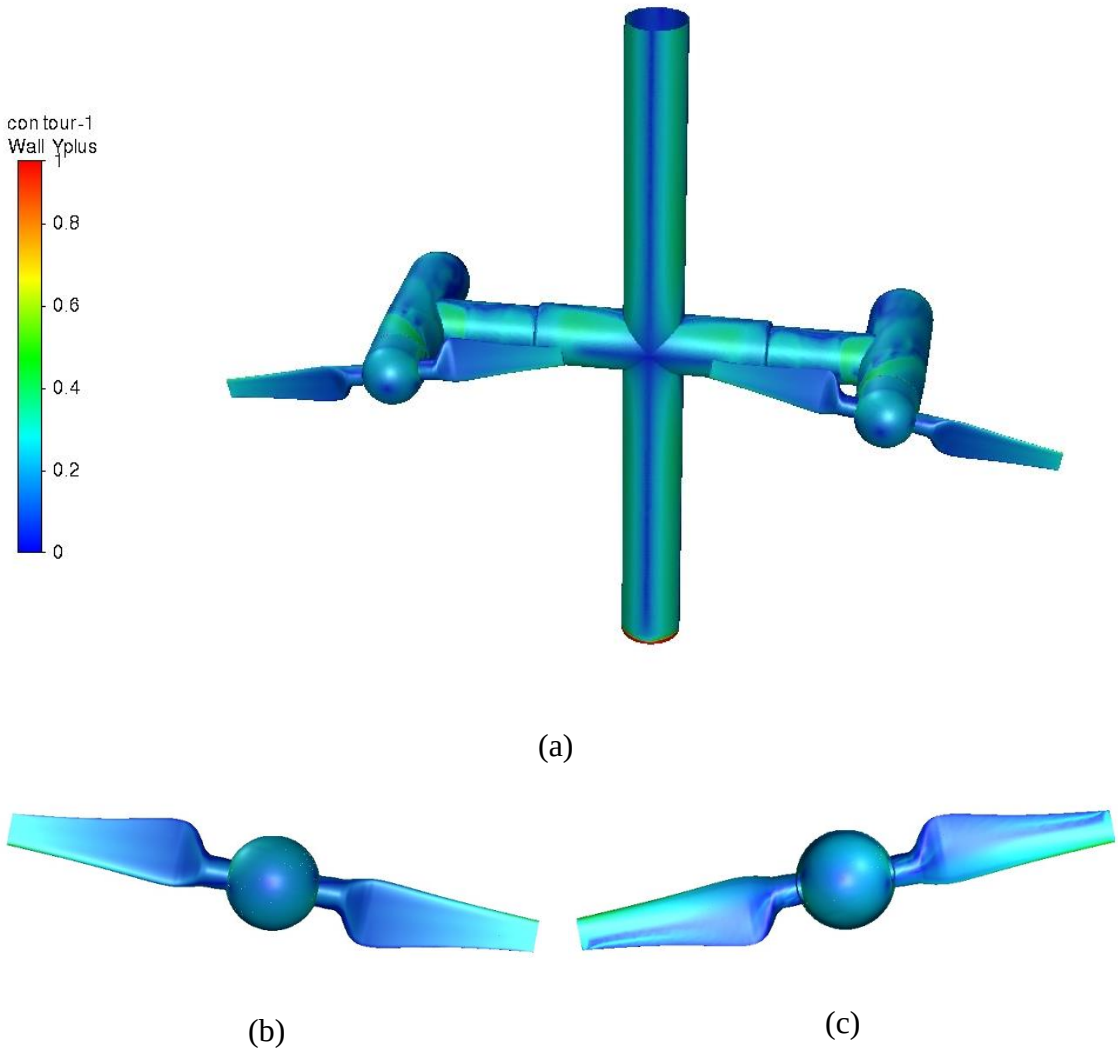

(a)

(b) (c)

Figure 6. Contour of wall y^+ on nacelle, rotor and supporting tower's walls (a), zoomed in view of the high pressure (b) and low pressure (c) side of the right rotor blade. Results were obtained using a TSR of 5.07 and lateral rotor spacing of $1.4d_T$.

Initially, an unstructured mesh consisting of tetrahedral and hexahedral cells was created for all simulations. Besides the refinement performed near the walls in the computational domain, additional refinements were conducted on the near, far, and full domains with the aim of tracking the tip vortices, shown in Figure 7.

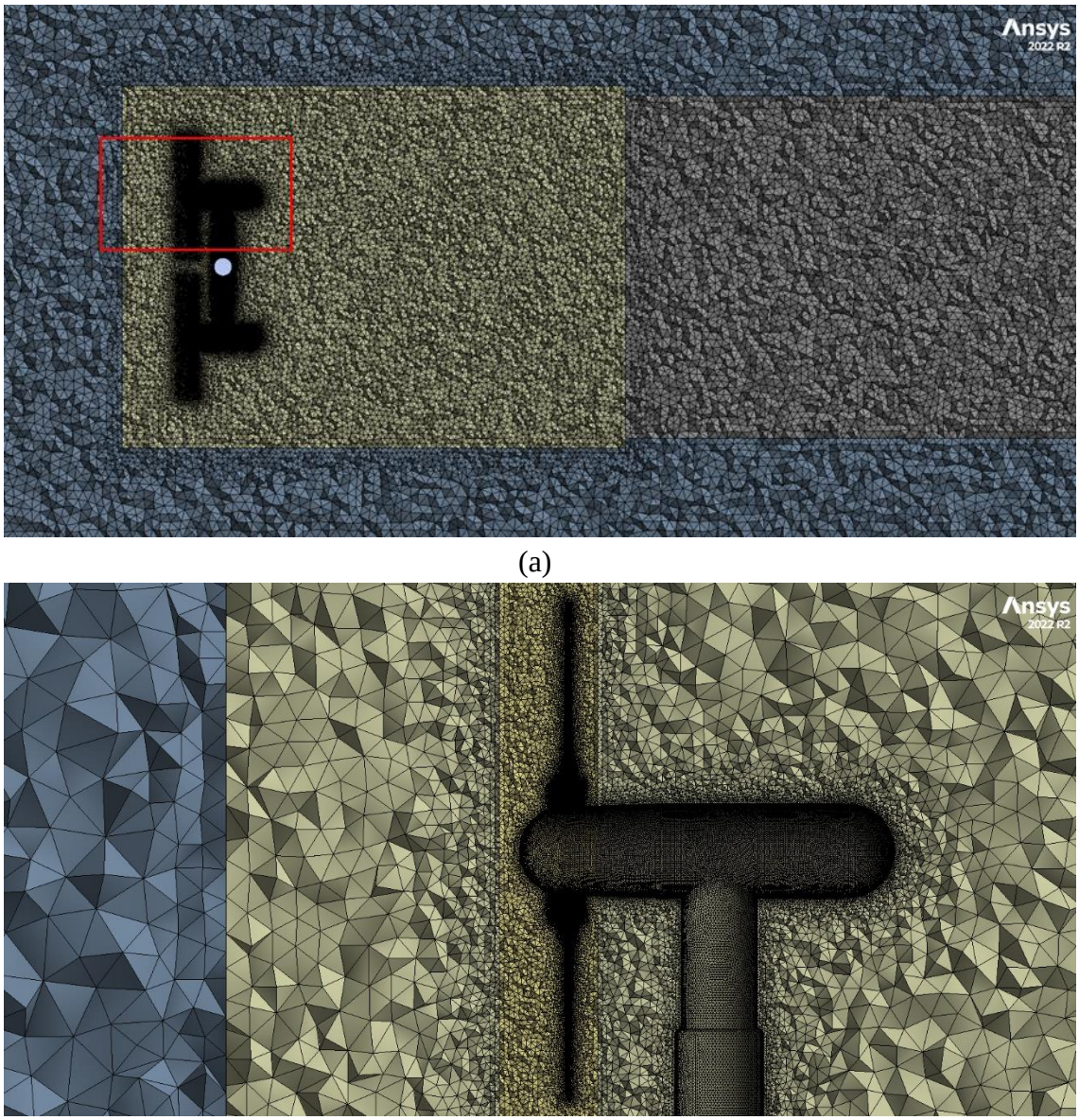

(a)

(b)

Figure 7. Illustration of the computational grid used in the simulations. (a) Showing refinements in the near and far wake, around rotors, cross-arms, and central supporting tower's walls. (b) Displays a detailed view of the enclosed region in the red box in (a).

After the initial meshes were created, a conversion to polyhedral cells mesh was performed. This operation decreased the number of cells to nearly half of that obtained in

the initial mesh composed of tetrahedral and hexahedral cells. In this study, three different polyhedral meshes were constructed by increasing the density of the mesh in all subdomains while monitoring C_p for convergence.

A hybrid initialization was used to start the simulations and immediately switch to transient conditions. Figure 8 illustrates the C_p signal from the beginning of the simulations and proves the importance of averaging this coefficient after a specific number of revolutions where the C_p becomes cyclic. In the beginning of the simulation, unreasonably high C_p values are recorded as the flow field presents no alteration yet. As the fluid continues to develop across the domain, the C_p starts to oscillate around a constant averaged C_p value. These oscillations are due to blade passing frequencies in front of tower structural support members. Since the RM1 model study here has two blades, there are two cycles per revolution in the C_p fluctuations.

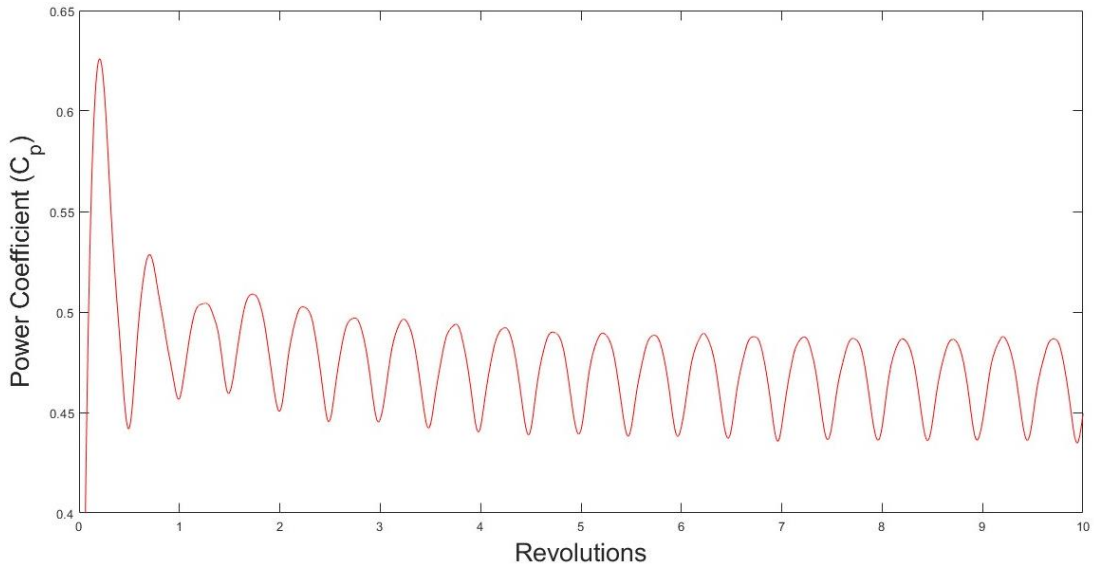

Figure 8. C_p signal as the flow field develops from initiation of the simulation. Signal corresponds for a TSR of 5.07, lateral rotor spacing of $1.4d_T$ and mesh with 21.93 million of polyhedral cells.

In the present study, data was recorded after the difference in the averaged C_p over one revolution between two consecutive revolutions was less than 1% and conserved within this value. Figure 9 presents the percentage difference in the averaged C_p between consecutive revolutions, showing that a minimum of 6 revolutions were needed in order to achieve an averaged cyclic C_p value as the difference was less than 1% and preserved within this value as the simulation processed.

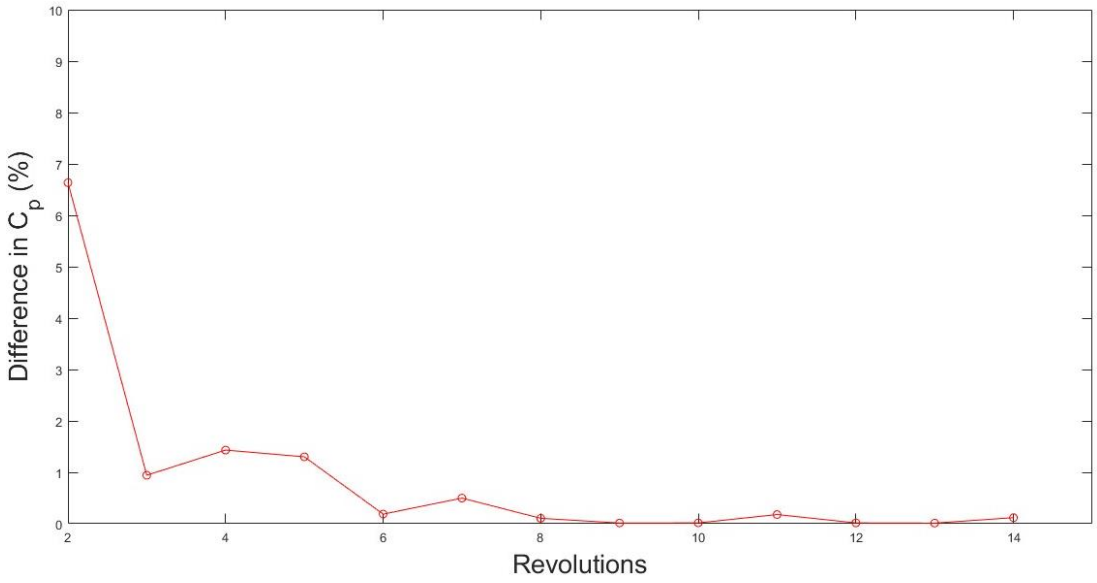

Figure 9. Percentage difference in the averaged C_p. Each point represents the average C_p value over one revolution starting from the previous revolution. Results corresponds for a TSR of 5.07, lateral rotor spacing of $1.4d_T$ and mesh with 21.93 million of polyhedral cells.

The final meshes created using polyhedral cells were labeled as coarse, medium, and fine mesh, with their respective total number of cells presented in Table 1. Experimental results obtained in [23] were used to compare the obtained numerical results. It should be noted that only results for the right rotor are discussed in the present study due to the uncertainties of accuracy of the experimental results for the left rotor, as discussed in [23].

Table 1. Averaged C_p for the three employed grids and absolute percent difference comparing to experimental values. All simulations were performed at a TSR of 5.07 and lateral rotor spacing of $1.4d_T$

	Cells (Millions)	**Averaged C_p (-)**	**Difference (%)**
Coarse	19.89	0.430	9.634
Medium	21.93	0.461	3.058
Fine	48.01	0.468	1.615
Experimental	--	0.476	--

All meshes studied, assured a y^+ of less than 1 around the walls of the rotors, cross-arms, and central supporting tower, ensuring that the boundary layer was correctly captured in these regions. In Figure 10, the C_p signal for two revolutions is presented showing the difference between the meshes used. All meshes were simulated for a $TSR = 5.07$ for validating the C_p with experimental data in [23]. The C_p was averaged over four revolutions for coarse, medium and fine meshes showing a difference of approximately 10, 3 and 2%, respectively, compared to experimental data (Table 1). In order to guarantee a good representation of the C_p while minimizing simulation time, the grid labeled as medium was chosen as ideal and used for future studies.

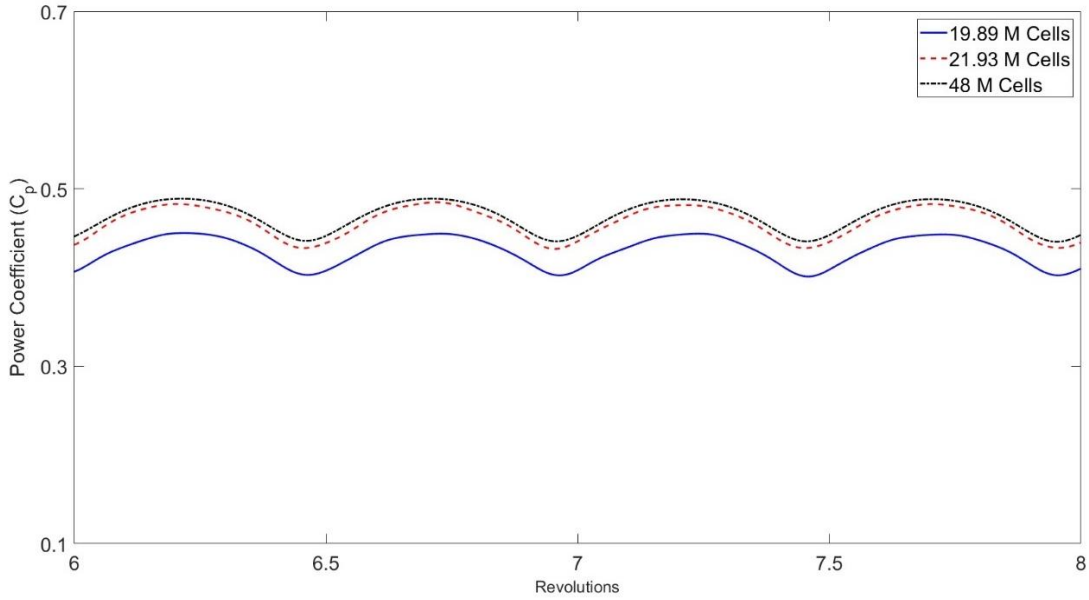

Figure 10. Comparison of C_p signal over two revolutions for the three considered meshes. All simulations were performed at a TSR of 5.07 and lateral rotor spacing of $1.4d_T$.

Next, a time-step independence study was performed to guarantee that the solution does not depend on time discretization. Following previous studies performed in [22], an initial time step of Δt = 0.0001 s was chosen as a baseline for the initial simulations. One smaller order in magnitude time step of Δt = 0.00001 s and a larger of Δt = 0.0003 s were also studied. The averaged C_p over four revolutions and the percentage difference is presented in Table 2.

Table 2. Averaged C_p for the three employed time steps and absolute percent difference with experimental values. All simulations were performed at a TSR of 5.07 and lateral rotor spacing of $1.4d_T$.

Time Step (s)	**Averaged C_p (-)**	**Difference (%)**
0.00001	0.463	2.73
0.0001	0.463	2.73
0.0003	0.461	3.15
Experimental	0.476	--

The Courant number (C) is a dimensionless value representing the number of mesh cells traveled by a particle at a given timestep. Is it defined as $C = u \cdot \Delta t/\Delta x$, where u is the velocity magnitude and Δx is the length between mesh elements. This variable is of utmost importance when analyzing transient effects and a small C needs to be guaranteed in order to correctly capture transient effects. All time steps used in the present simulations ensured a Courant number less than 1 in all regions as far as possible, complying with the turbulence model's requirements, assuring the correct unsteady evolution of the flow, and capturing transient phenomena, such as tip vortices. A time-step of Δt = 0.0003 s was finally selected for the following simulations as the C_p coefficient was within a 3% difference compared to experimental data while minimizing simulation time needed for one revolution from approximately 29800 to 1000 time steps (Δt) when using steps of Δt = 0.00001 s and Δt = 0.0003 s, respectively.

3.2. TSR Versus C_p – Validation against experimental data

Two additional TSR (λ) were simulated and compared against experimental data to demonstrate the advantage that the $SST\ k-\omega$ turbulence model has when simulating

complex flows, especially those with separated flow induced by adverse pressure gradients when stall happens. [23]. A TSR of λ = 3 and λ = 7.6 were selected to predict the C_p during relatively slow and fast blade rotational speeds.

Table 3. Comparison of averaged C_p for three TSR numerically studied versus experimental data [23]. Data represents the absolute percent difference for simulation using a lateral rotor spacing of $1.4d_T$.

TSR, λ (-)	**Averaged C_p (-)**	**Experimental C_p (-)**	**Difference (%)**
3	0.310	0.320	3.125
5.07	0.461	0.476	3.153
7.6	0.382	0.368	3.804

Table 3 shows the predicted C_p for all TSR studies and the measured experimental values. Results exhibit a difference of approximately 3% for a $TSR = 3$ and a difference of 4% for a $TSR = 7.6$. All numerical results are in acceptable 5% range with experimental data illustrating the advantage and ability of the $SST\ k-\omega$ turbulence model of dealing with a variety of challenging flows.

Numerical results closely matched experimental results and the expected behavior on the RM1 performance curve, observed in Figure 11, where the C_p starts to increase with higher TSR until reaching its maximum value. As the TSR continues to increase, the C_p starts to decrease in value. This is attributed to the angle of attack changing from its optimal value for most of the airfoil along the blade span, as previously found in similar studies [20]. CFD results also display that maximum C_p for the TSR studied was achieved at $\lambda = 5.07$, closely agreeing with experiments and similar numerical studies in [86].

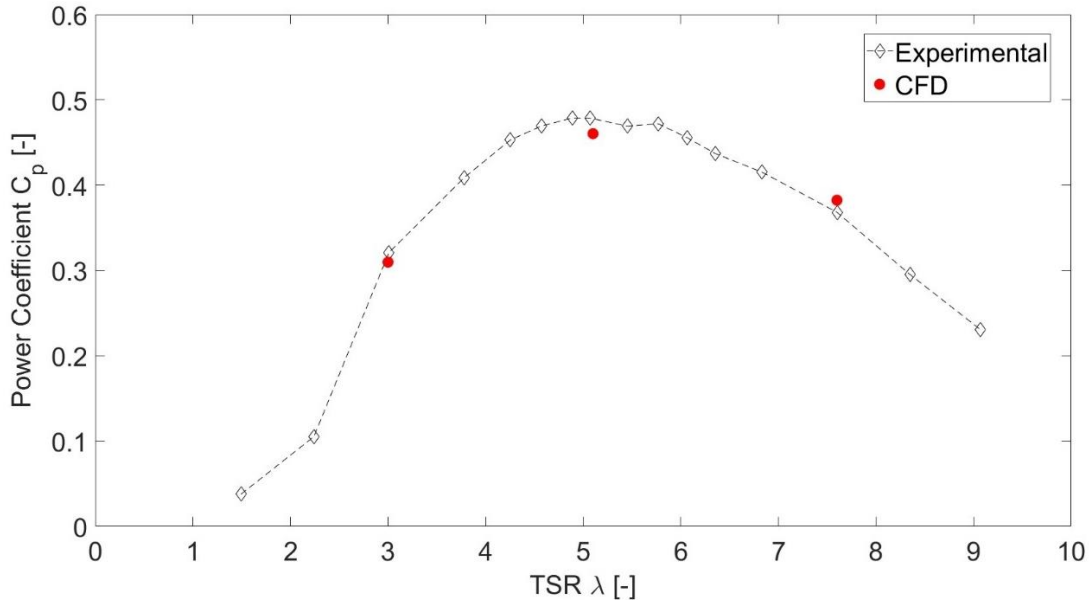

Figure 11. Experimental data [23] of C_p as a function of TSR overlaying CFD results for all TSR studied and lateral rotor spacing of $1.4d_T$.

A TSR of λ = 7.6 was studied to predict the performance when stall occurs causing higher drag and reduction in lift. Table 4 displays the instantaneous drag and lift coefficients monitored in the simulations for all TSRs at the same blade position and averaged along the blades spam. As it can be noted, a maximum lift coefficient is achieved for optimum TSR (λ = 5.07) while on the other hand, the drag coefficient is maximum for λ = 7.6 due to expected stall under this high rotational speed.

Table 4. Blade averaged lift (C_L) and drag coefficients (C_D) for all TSRs studied. Values correspond to a blade azimuth angle of 90° and match position of values reported in Table 3.

TSR, λ (-)	**Lift Coefficient C_L (-)**	**Drag Coefficient C_D (-)**
3	0.0116	0.5641
5.07	0.0220	0.8375
7.6	0.0097	1.0720

The skin friction coefficient (C_f) is a dimensionless variable relating the shear stress at the wall (τ_w) normalized by the dynamic pressure of the free stream (P_D), $C_f = \tau_w / P_D$. The dynamic pressure is defined as $P_D = 1/2 \cdot \rho \cdot u_e$, where ρ and u_e are the values of the density and the velocity at the edge of the boundary layer [87]. When there is high attachment of the flow to the boundary, wall shear stresses are high thus, the skin friction coefficient increases. In contrast, when the flow is detached from the boundary, low wall shear stresses are presented and thus, the skin friction coefficient decreases. Skin friction coefficient contours along the rotor's blades are presented in Figure 12 for the three different TSR studied to visualize the detachment of the fluid on the blades. As seen in Figure 12, flow separation decreases as the TSR increases, visualized by the decreasing dark blue regions near the root of the blades, with highest detachment for a $\lambda = 3$.

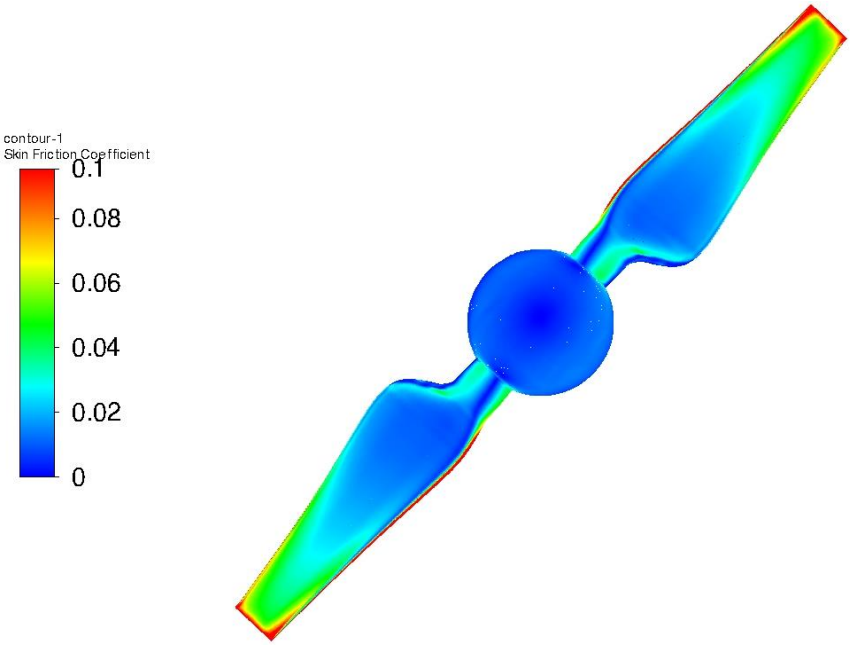
contour-1
Skin Friction Coefficient
0.1
0.08
0.06
0.04
0.02
0

(a)

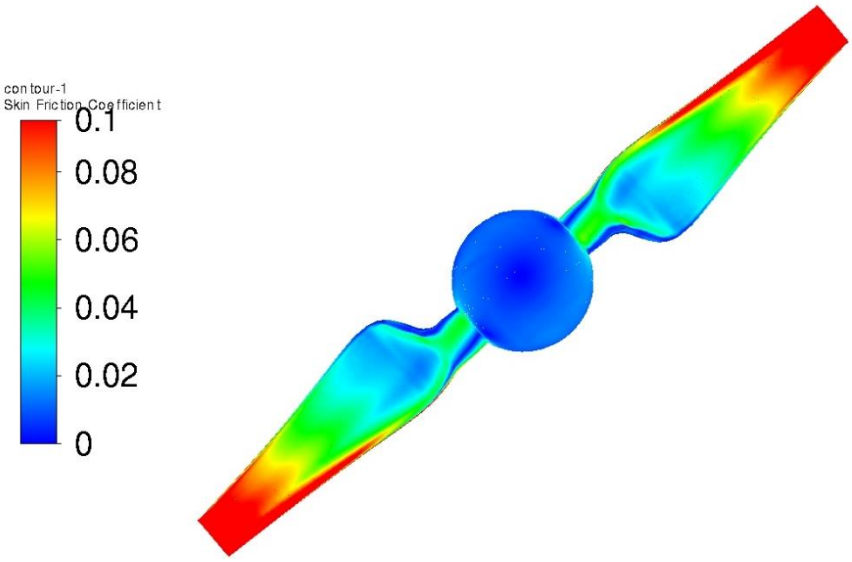
contour-1
Skin Friction Coefficient
0.1
0.08
0.06
0.04
0.02
0

(b)

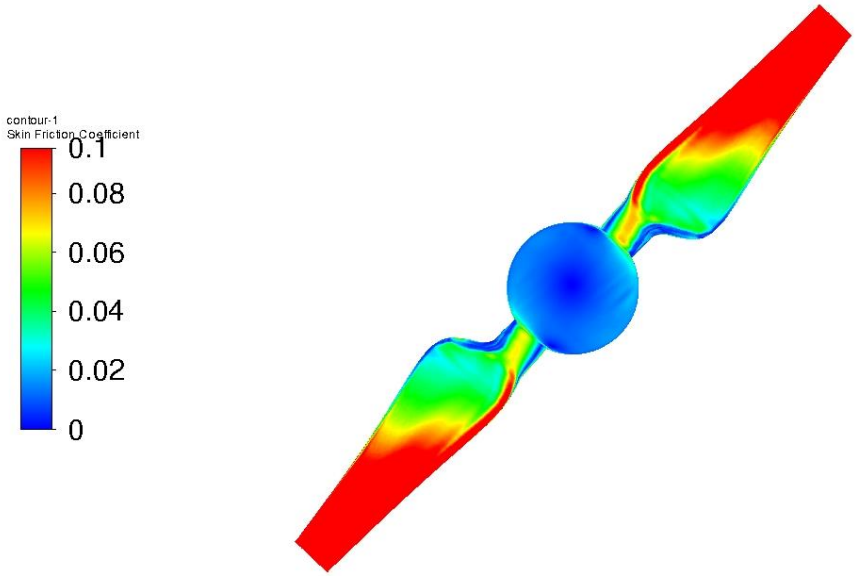

(c)

Figure 12. Skin friction contours along the rotor's surface. (a) TSR = 3, (b) TSR = 5.07 and (c) TSR = 7.6. Simulations were run for a lateral rotor spacing of $1.4d_T$.

A time series of C_p for all three TSR studied is visualized in Figure 13, where is apparent that the torque, which ultimately contributes towards power production and influences the C_p values, changes as a function of the blade azimuth position. The fluctuating power production is a result of blades passing in front of turbine tower support structures, in this case, the horizontal support arms extending from the central tower to each nacelle. This behavior occurs, as expected, for all TSR studied.

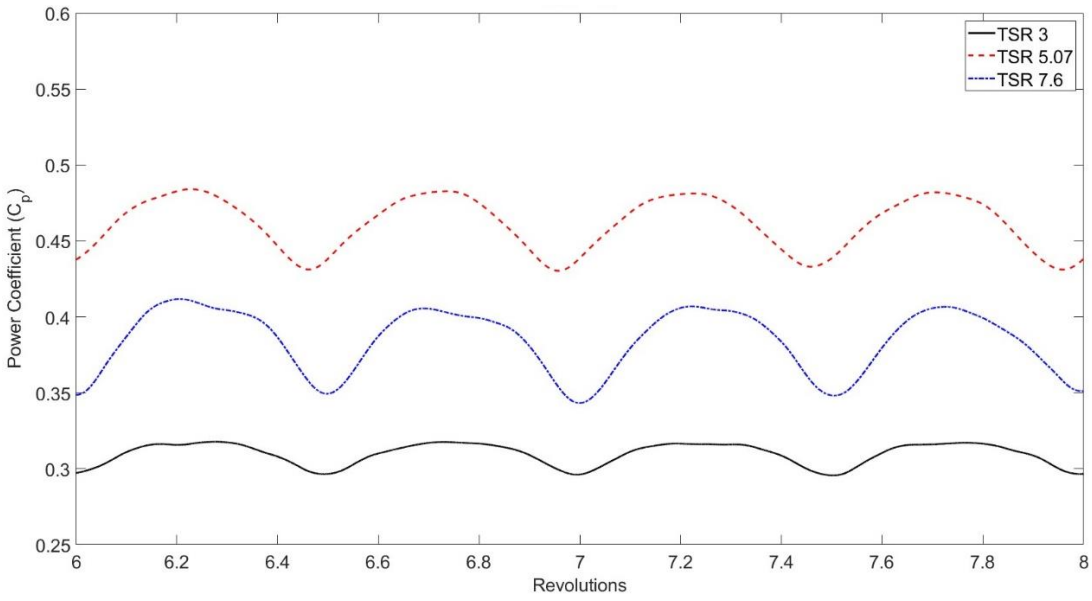

Figure 13. Variation of the C_p signal as a function of number of revolutions for all TSR studied and lateral rotor spacing of $1.4d_T$.

3.3. Inflow and Wake Visualization

To visualize the kinematics of the flow across the domain, Figure 14 shows the horizontal velocity contour at hub height from distances of $X/d_T = -2$ upstream to $X/d_T = 10$ for a TSR of $\lambda = 5.07$. It is evident how placing the turbine and supporting structure causes a disturbance not only in the upstream region (i.e., induction zone) but also in the downstream region of the turbine (i.e., turbulent wake). The flow decelerates as it approaches the turbine blades, power extraction from the incoming flow begins, and finally creates a turbulent wake. Moreover, close to the blade's tip, the shed tip vortices are captured and displayed by the intense red regions showing the inhomogeneity of the flow in these regions.

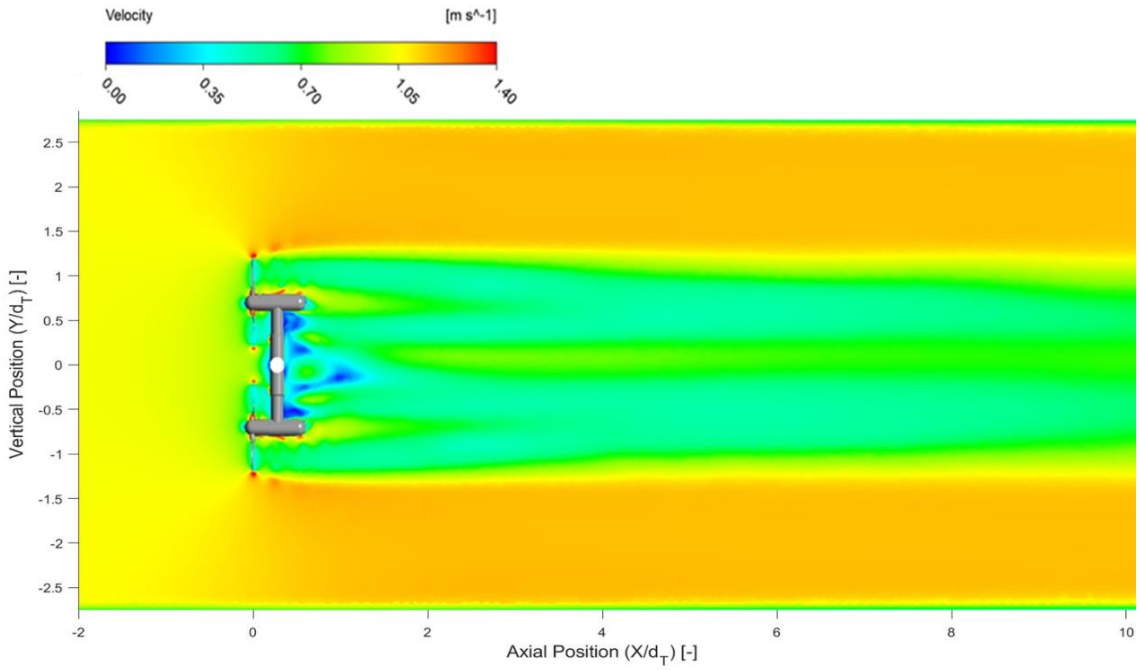

Figure 14. Horizontal velocity contour at hub height for a TSR of 5.07 and lateral rotor spacing of $1.4d_T$. Flow is left to right.

Figure 15 shows the velocity deficit profile at hub height for the right rotor as well as for the center tower obtained experimentally in [23] from distances of $X/d_T = -5$ up to $X/d_T = 16$ and by the numerical simulations performed from $X/d_T = -5$ up to $X/d_T = 8$. The velocity deficit profiles give an idea of the velocity recovery in the wake of a device. Although the results obtained by $k - \omega\ SST$ model had good agreement with experimental results for the C_p, the same agreement was not true for characterizing the full wake. Comparable results were found by similar numerical simulations performed using the same turbulence model in [22], where authors found the inadequate capture of the wake dissipation rate using different RANS models.

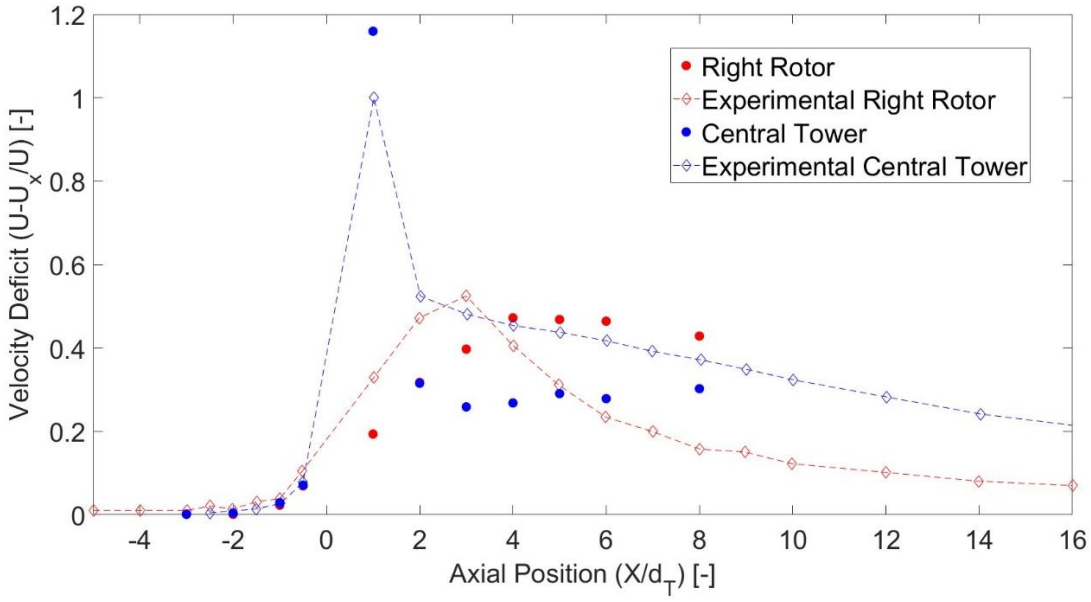

Figure 15. Comparison of hub height velocity deficit for right rotor and central tower. Results correspond to a TSR of 5.07 and lateral rotor spacing $1.4d_T$.

Figure 15 indicates appreciable differences in the velocity deficit for the wake starting from a distance of $X/d_T = 1$. In the upstream region of the turbine, numerical results were in good concordance with experimental data as they differ by less than 5%.

Although the results did not completely capture the wake dynamics in magnitude correctly, the trend of the velocity deficit is similar to the experimental data and hence will be further explained. From Figure 15 it is apparent how, as previously stated, the RM1 starts to affect the inflow (upstream) velocities, decelerating the fluid and increasing the velocity deficit. In the near wake, the fluid exhibits higher velocity deficits due to momentum transfer between the fluid and the device. This region is characterized by a strong vortex formation which starts to mix with the bypass flow further downstream, recovering the velocity and hence the velocity deficit decreases. The largest velocity deficit

is obtained for the near wake of the central tower where strong vortices and detachment of the flow occur right behind the structure. Vortices caused by rotor and nacelle walls are higher in quantity and magnitude compared to vortices shed by the central tower, as visualized in Figure 16, where isosurfaces of normalized q-criterion are used to visualize the vortices detached, colored by the velocity of the fluid.

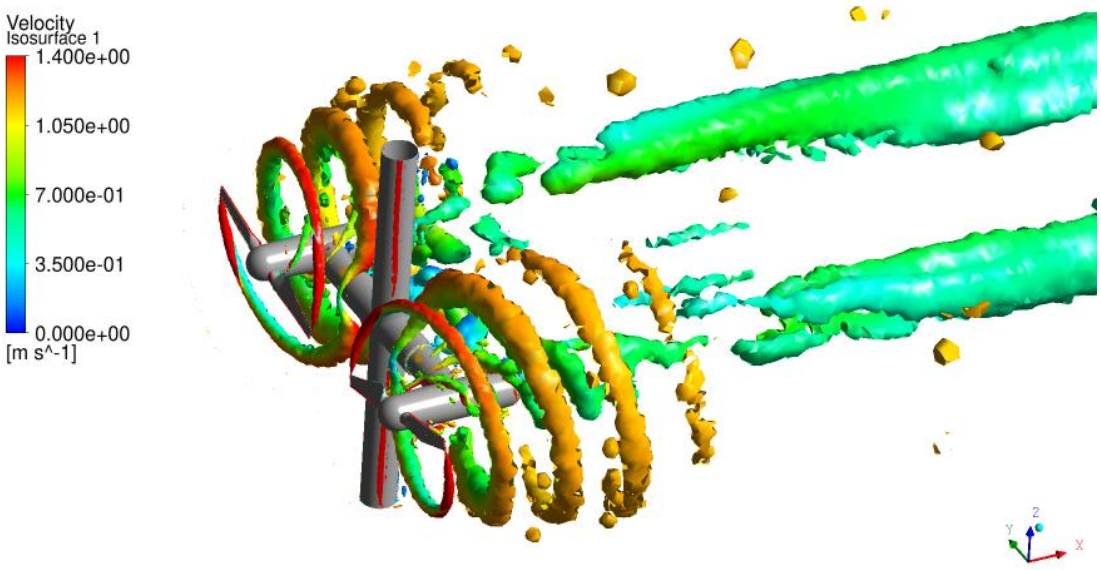

Figure 16. Normalized isosurface of Q-Criterion color with velocity for a TSR of 5.07 and lateral rotor spacing of $1.4d_T$. Flow is left to right.

Focusing on the right rotor in Figure 15, the velocity deficit in the wake starts to increase as the fluid moves away from the rotor's power extraction plane, reaching a velocity deficit peak of 47.20% at $X/d_T = 4$. After this point, the fluid mixes with the bypass flow and begins to gradually recover. The wake predicted by the current numerical results shows a recovery of 57.5% of the upstream velocity at $X/d_T = 8$ compared to

approximately 84.3% reported experimentally in [23] at the same position. This behavior can be attributed to multiple reasons such as the inappropriate estimation of the dissipation rate by URANS models like the $k-\omega\ SST$, as previously found in studies like [22], the assumption on dealing with isotropic turbulence imposed by the Boussinesq hypothesis, which all RANS models assume and the lack of resolving small eddies, which can be solved by using higher order turbulence models such as DES or LES. Also, it is key to highlight that the mesh used for studying the wake was chosen by the independency study presented in section 3.1., where the C_p was selected as the parameter for convergence and possibly ignoring the effect that the spatial discretization of the regions behind the rotor might have on the wake representation.

3.4. Influence of Rotor Spacing

The maximum power that a turbine can extract in a tidal channel is dependent on its channel blockage ratio, i.e., the ratio of the frontal swept area of the turbine to the cross-sectional area of the channel. The theoretical model of Garrett and Cummins indicated that the power extraction increases as the blockage in the channel expand with the installation of more turbines laterally [88]. However, in practice, this does not hold if too many turbines are added along the channel cross-section, as the efficiency decreases due to the reduction of the energy flux through the channel, discussed in more detail in [89]. Also in reality, a considerable portion of a tidal channel cross section must also be unblocked to allow for navigation of vessels and so forth, limiting the number of turbines that can be placed across the channel's width. Due to this limitation, it is key to find the optimal spacing between the turbines that maximizes power production while minimizing the width occupied by the

devices. For this reason, in this study, three different lateral spacings were studied corresponding to $L/d_T = 1.2, 1.4$ and 1.6, where L is the axial distance between the center of each rotor, as seen in Figure 17. As the RM1 contains only two rotors deployed from a single tower, the blockage ratio was kept constant, allowing one to focus solely on the effect of turbine spacing.

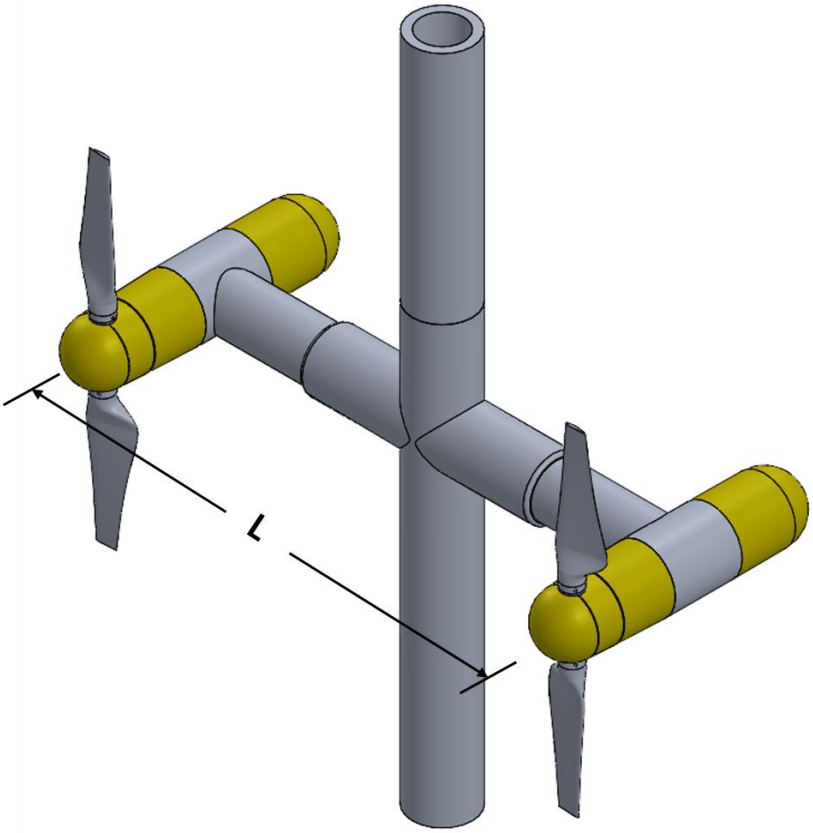

Figure 17. Axial distance between the center axis of rotation for each rotor.

All parameters selected when meshing the three different lateral spacing domains were constant, guaranteeing that the meshes created were comparable to each other. Table 5 presents the C_p for all three cases studied, showing a tendency of a higher C_p as the two rotors are spaced farther apart.

Table 5. C_p for three lateral rotor spaces numerically studied for a TSR of 5.07. Right column shows the difference in numerical results compared to case with $1.4d_T$.

Lateral Axial Spacing L/d_T (-)	**Power Coefficient C_p (-)**	**Difference from $1.4d_T$ case (%)**
1.2	0.449	-2.6%
1.4	0.461	0.0%
1.6	0.483	4.8%

Increasing the lateral spacing from $L/d_T = 1.2$ to 1.4 generated an increase of approximately 3% on the C_p, while the increase from $L/d_T = 1.4$ to 1.6 caused an increment of 5% on the C_p. This behavior can be explained by the choking effect, i.e., reduced flow through the swept area of both rotors. To better visualize this, velocity contours at a vertical plane at the rotor's center are presented in Figure 18, comparing the different flow fields obtained for all three lateral spacing.

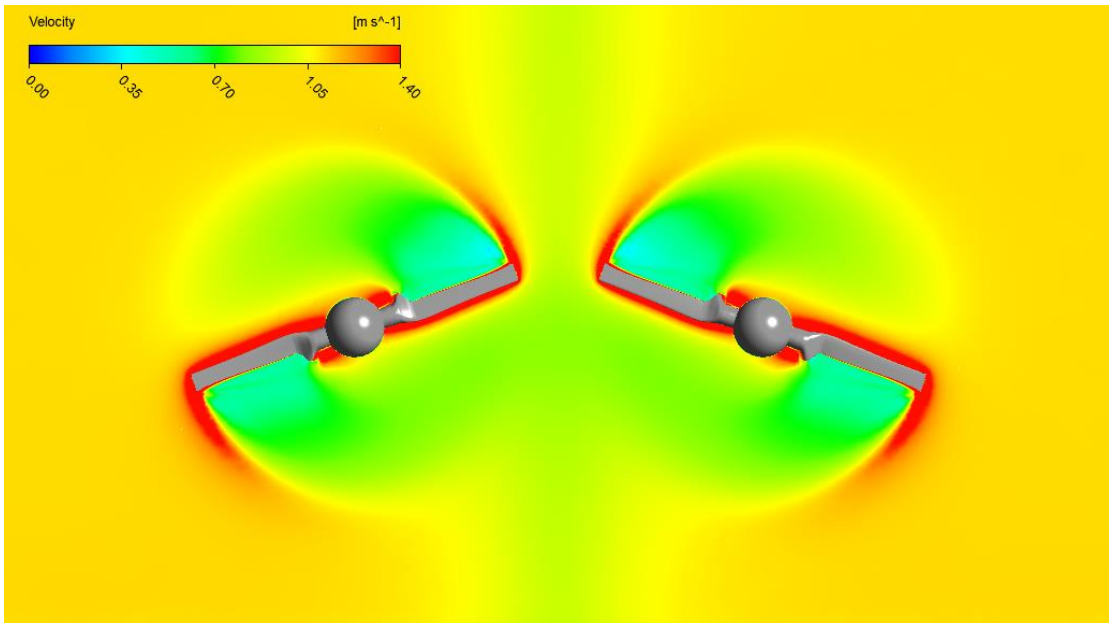

(a)

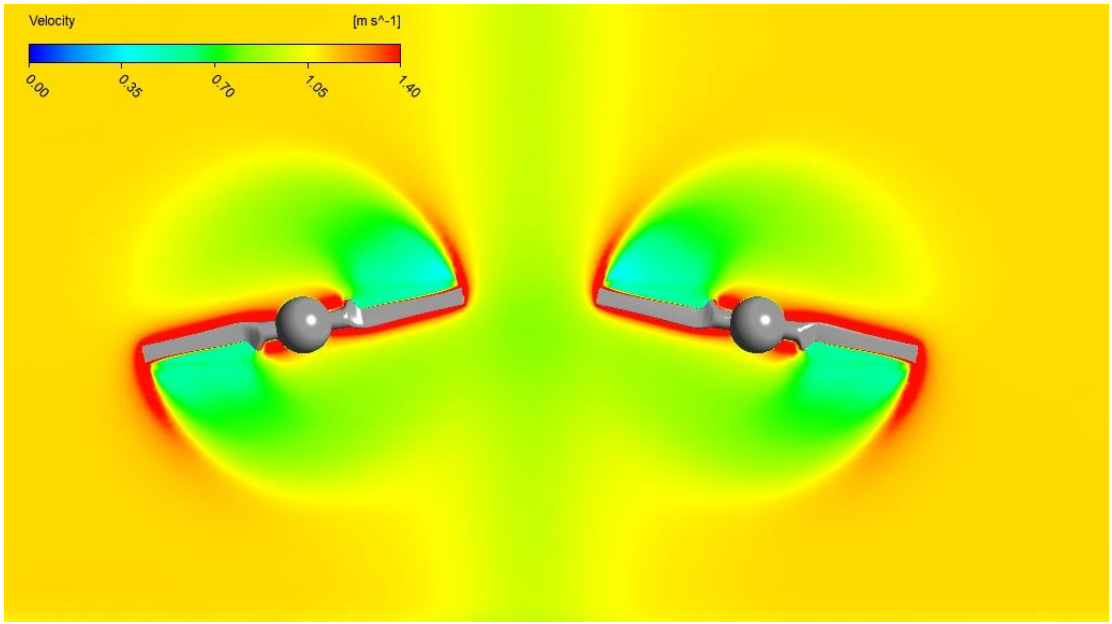

(b)

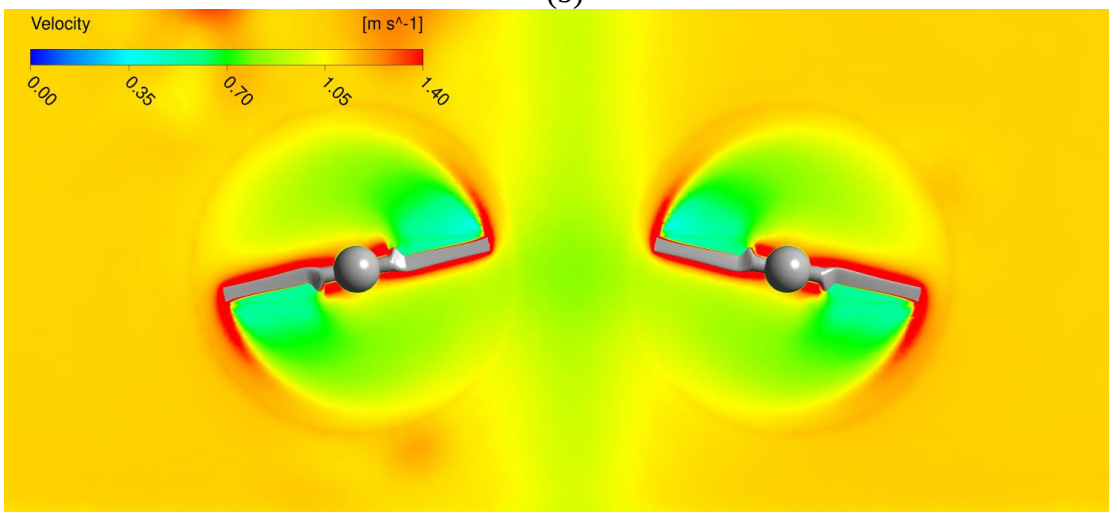

(c)

Figure 18. Velocity contours at vertical plane in rotor centers for lateral spacing of (a) $1.2d_T$, (b) $1.4d_T$ and (c) $1.6d_T$. Results were obtained for a TSR of 5.07.

As seen in Figure 18, the velocity field around the rotors is affected by the reduction in the lateral spacing between both rotors. While the rotors are placed closer together, the flow through each rotor swept area is affected by each other, reducing the velocities in this

section due to an increase in blockage, and therefore choking the fluid that crosses this section. This reduction in fluid's kinetic energy around the rotors plane causes a lower energy extraction by the blades and therefore the overall power production decreases. Similar results have been found in similar studies [83, 90, 91].

4. Conclusions and Future Work

In this study, numerical simulations based on the *k-ω SST* turbulence model and the sliding mesh technique were performed for a 1:40 full geometric scaled model of the DOE RM1 turbine, a dual-rotor axial flow turbine with counter-rotating rotors, each with a diameter $d_T = 0.5$ m. Results suggested that when numerically studying the performance of turbines a minimum of six revolutions are needed for the power coefficient to converge. For this reason, power coefficients should be averaged after reaching this condition, eliminating high power coefficients obtained when the flow has not yet developed sufficiently through the computational domain.

The ability of the $k-\omega\ SST$ turbulence model of dealing with low and high detached flow was proven by simulating three different TSR that encompassed a slow ($\lambda = 3$), optimal ($\lambda = 5.07$) and fast ($\lambda = 7.6$) blade rotation. All numerical results obtained for C_p exhibited a percentage difference of less than 5% compared to experimental data. Skin friction contours along the blade's walls were presented to show the detachment of the flow under each TSR studied. Although numerical results obtained by $k-\omega\ SST$ model were in good agreement with experimental results for C_p, the same was not achieved when characterizing the full wake as numerical results differ to experimental data. This behavior

was accredited to an inappropriate estimation of the dissipation rate by URANS models like the $k-\omega\,SST$ model due to the assumption of isotropic turbulence imposed by the Boussinesq hypothesis in all RANS models, and lack of resolving small eddies.

Impact of rotor axial spacing on the mechanical performance of the turbine was investigated by simulating three different cases of $1.2d_T$, $1.4d_T$ and $1.6d_T$. It was found that this spacing had a significant impact on power performance of this turbine as numerical results show that C_p increases by way of rotors being spaced farther apart. A maximum of 5% growth in performance was achieved by increasing the spacing from $1.4d_T$ to $1.6d_T$. This behavior was attributed to the choking effect (i.e., a reduction of the flow through the swept area of the rotors). These findings have important implications for design and optimization of this type of tidal turbine as it can be used as a guideline when designing future tidal turbines, with the potential to increase the power output and efficiency of these devices.

There are several avenues for future work based on the findings of this study. Initially, the study focused on the influence of rotor spacing on power performance, but there are additional factors that could be investigated, such as the impact of the cross-sectional area of the supporting arms and central tower, depth of installation, and asynchronous rotor rotation. Furthermore, in order to reduce computational resources needed and time, a symmetry condition for the top wall of the computational domain was set, neglecting the effects of free surface deformation. This assumption can possibly affect the correct wake capturing as free-surface effects in the form of standing waves, or decreased water surface above the turbine, are ignored. Additionally, although computational resources needed

would be extremely high, sophisticated turbulence models such as LES and DNS could be potentially implemented for wake characterization. These models would be able to simulate (LES) or solve (DNS) small eddies providing an improved representation of wake recovery.

Bibliography

[1] A. J. Cohen, "Estimates and 25-year trends of the global burden of disease attributable to ambient air pollution: An analysis of data from the Global Burden of Diseases Study 2015," *The Lancet*, p. 1907–1918, 2017.

[2] U. Nations, "Climate Action," United Nations, [Online]. Available: https://www.un.org/en/climatechange/science/key-findings#physical-science. [Accessed 17 November 2022].

[3] REN21, "Renewables 2022 Global Status Report," Paris, 2022.

[4] IEA, "Renewables 2021 Anaysis and forecasts to 2026," 2021.

[5] A. Qaza, F. Hussain, N. A. Rahim, G. Hardaker, D. Alghazzawi, K. Shaban and K. Haruna, "Towards Sustainable Energy: A Systematic Review of Renewable Energy Sources, Technologies, and Public Opinions," *IEEE Access*, vol. 7, pp. 63837-63851, 2019.

[6] O. Demirtas, "Evaluating the Best Renewable Energy Technology For Sustainable Energy Planning," *International Journal of Energy Economics and Policy*, vol. 3, no. 4, pp. 23-33, 2013.

[7] Y. Liu, Y. Li, F. He and H. Wang, "Comparison study of tidal stream and wave energy technology development," *Renewable and Sustainable Energy Reviews*, vol. 76, pp. 701-716, 2017.

[8] J. V. Hernandez Fontes, L. M. Martinez, A. Wojtarowski, J. L. Gonzalez Mendoza, R. Landgrave and R. Silva, "Is ocean energy an alternative in developing regions? A case study in Michoacan, Mexico," *Journal of Cleaner Production*, vol. 266, 2020.

[9] A. LiVecchi, A. Copping, A. Jenne, A. Gorton, R. Preus, G. Gill, R. Robichaud, R. Green, S. Geerlofs, S. Gore, D. Hume, W. McShane, C. Schmaus and H. Spence, "Powering the Blue Economy; Exploring Opportunities for," U.S. Department of Energy, Washington, D.C., 2019.

[10] L. Kilcher, M. Fogarty and M. Lawson, "Marine Energy in the United States: An Overview of Opportunities," National Renewable Energy, Golden, 2021.

[11] Z. Wang, R. Carriveau, D. Ting, W. Xiong and Z. Wang, "A review of marine renewable energy storage," *International Journal of Energy Research,* vol. 43, pp. 6108-6150, 2019.

[12] A. Hoseyni-Chime and P. C. Malte, "HYDROKINETIC TURBINES AT HIGH BLOCKAGE RATIO," in *Marine Energy Technology Symposium*, Seattle, 2014.

[13] C. A. Consul, R. H. J. Willden and S. C. McIntosh, "Blockage effects on the hydrodynamic performance of a marine cross-flow turbine," *Philosophical Transactions of the Royal Society A,* vol. 371, pp. 1-16, 2013.

[14] T. Kinsey and G. Dumas, "Impact of channel blockage on the performance of axial and," *Renewable Energy,* vol. 103, pp. 239-254, 2017.

[15] H. Ross and B. Polagye, "An experimental assesment of analytical blockage corrections for turbines," *Renewable Energy,* vol. 152, pp. 1328-1341, 2020.

[16] O. Pacot, D. Pettinaroli, J. Decaix and C. Munch-Alligne, "Cost-effective CFD simulation to predict the performance of a hydrokinetic turbine farm," in *IOP Conference Series: Earth and Environmental Science,* 2019.

[17] J. Riglin, F. Carter, N. Oblas, W. C. Schleicher, C. Daskiran and A. Oztekin, "Experimental and numerical characterization of a full-scale portable hydrokinetic turbine prototype for river applications," *Renewable Energy,* vol. 99, pp. 772-783, 2016.

[18] H. W. Ren, F. A. Z. M. Saat, F. S. Anuar, M. A. A. Wahap, E. M. Tokit and T. B. Tuan, "Computational Fluid Dynamics Study of Wake Recovery for Flow Across Hydrokinetic Turbine at Different Depth of Water," *CFD Letters,* vol. 13, no. 2, pp. 62-76, 2021.

[19] A. Benavides-Morán, L. Rodríguez-Jaime and S. Laín, "Numerical Investigation of the Performance, Hydrodynamics, and Free-Surface Effects in Unsteady Flow of a Horizontal Axis Hydrokinetic Turbine," *Processes,* vol. 10, no. 69, pp. 1-17, 2022.

[20] T. Javaherchi, N. Stelzenmuller, J. Seydel and A. Aliseda, "EXPERIMENTAL AND NUMERICAL ANALYSIS OF A SCALE-MODEL HORIZONTAL AXIS HYDROKINETIC TURBINE," in *2nd Marine Energy Technology Symposium,* Seattle, 2014.

[21] T. Javaherchi, N. Stelzenmuller and A. Aliseda, "Experimental and numerical analysis of the performance and wake of a scale-model horizontal axis marine hydrokinetic turbine," *JOURNAL OF RENEWABLE AND SUSTAINABLE ENERGY,* vol. 9, 2017.

[22] C. M. Niebuhr, S. Schmidt, M. van Dijk, L. Smith and V. S. Neary, "A review of commercial numerical modelling approaches for axial hydrokinetic turbine wake analysis in channel flow," *Renewable and Sustainable Energy Reviews,* vol. 158, 2022.

[23] C. Hill, V. S. Neary, M. Guala and F. Sotiropoulos, "Performance andWake Characterization of a Model Hydrokinetic Turbine: The Reference Model 1 (RM1) Dual Rotor Tidal Energy Converter," *Energies,* vol. 13, no. 19, p. 5145, 2020.

[24] E. E. Lust, K. A. Flack and L. Luznik, "Survey of the near wake of an axial-flow hydrokinetic turbine in the presence of waves," *Renewable Energy,* vol. 146, pp. 2199-2209, 2020.

[25] P. R. Spalart and S. R. Allmaras, "A one-equation turbulence model for aerodynamic flows," *La Recherche Aerospatiale,* pp. 5-21, 1994.

[26] M. D. Polewski and P. G. A. Cizmas, "Several Cases for the Validation of Turbulence Models Implementation," *Applied Sciences,* vol. 11, no. 8, p. 3377, 2021.

[27] B. E. Launder and D. B. Spalding, Lectures in Mathematical Models of Turbulence, London: Academic Press, 1972.

[28] F. R. Menter, "Review of the shear-stress transport turbulence model experience from an industrial perspective," *International Journal of Computational Fluid Dynamics,* vol. 23, no. 4, pp. 305-316, 2009.

[29] J. Wilcox, Wilcox, La Canada: DCW Industries, Inc., 1998.

[30] ANSYS, Inc., Ansys Fluent Theory Guide, Canonsburg: ANSYS, 2023.

[31] D. C. Wilcox, "Formulation of the k-w Turbulence Model Revisited," *American Institute of Aeronautics and Astronautics,* vol. 46, no. 11, pp. 2823-2838, 2008.

[32] F. R. Menter, "Two-Equation Eddy-Viscosity Turbulence Models for Enfineering Applications," *American Institute of Aeronautics and Astronautics,* vol. 32, no. 8, pp. 1598-1605, 1994.

[33] J. R. Ball and A. Jameson, "Explicit filtering and exact reconstruction of the sub-filter stresses in large eddy simulation," *Journal of Computational Physics,* vol. 306, pp. 117-136, 2015.

[34] A. Rezaeiha, H. Montazeri and B. Blocken, "On the accuracy of turbulence models for CFD simulations of vertical axis wind turbines," *Energy,* vol. 180, pp. 838-857, 2019.

[35] H. R. Karbasian, S. A. Moshizi and M. J. Maghrebi, "Dynamic Stall Analysis of S809 Pitching Airfoil in Unsteady Free Stream Velocity," *Journal of Mechanics,* vol. 32, no. 2, pp. 227-235, 2015.

[36] M. Zhao, D. Wan and Y. Gao, "Comparative Study of Different Turbulence Models for Cavitational Flows around NACA0012 Hydrofoil," *Journal of Marine Science and Engineering,* vol. 9, no. 7, p. 742, 2021.

[37] M. A. Abdelrahman, O. E. Abdellatif, M. Moawed, A. Eliwa and S. Mišák, "The CFD performance analysis for horizontal axis wind turbine with different blade shapes and tower effect," in *16th International Scientific Conference on Electric Power Engineering (EPE)*, Kouty nad Desnou, 2015.

[38] O. D. Lopez Mejia, O. E. Mejia, K. M. Escorcia, F. Suarez and S. Lain, "Comparison of Sliding and Overset Mesh Techniques in the Simulation of a Vertical Axis Turbines for Hydrokinetic Applications," *Processes,* vol. 9, p. 1933, 2021.

[39] E. O. do Nascimento, E. A. de Freitas, E. F. Lins and J. R. P. Vaz, "Performance assessment of an Indalma hydro-turbine," *SN Applied Sciences,* vol. 2, p. 2156, 2020.

[40] G. N. Barakos, T. Fitzgibbon, A. N. KUSYUMOV, S. A. KUSYUMOV and S. A. MIKHAILOV, "CFD simulation of helicopter rotor flow based on unsteady actuator disk model," *Chinese Journal of Aeronautics,* vol. 33, no. 9, pp. 2313-2328, 2020.

[41] T. Blackmore, W. M. J. Batten and A. S. Bahaj, "Influence of turbulence on thewake of a marine currentturbine simulator," *Proceedings of the Royal Society A*, vol. 470, 2014.

[42] M. Tzimas and J. Prospathopoulos, "Wind turbine rotor simulation using the actuator disk and actuator line methods," *Journal of Physics: Conference Series*, vol. 753, 2016.

[43] C. E. Badoe, M. Edmunds, A. J. Williams, A. Nambiar, B. Sellar, A. Kiprakis and I. Masters, "Robust validation of a generalised actuator disk CFD model for tidal turbine analysis using the FloWave ocean energy research facility," *Renewable Energy*, vol. 190, pp. 232-250, 2022.

[44] I. O. Sert, S. C. Cakmakcioglu, O. Tugluk and N. Sezer-Uzol, "The CFD Investigation of Two Non-Aligned Turbines Using Actuator Disk Model and Overset Grids," *Journal of Physics: Conference Series*, vol. 524, 2014.

[45] X. Liu, S. Yan, Y. Mu, X. Chen and S. Shi, "CFD and Experimental Studies on Wind Turbines in Complex Terrain by Improved Actuator Disk Method," *Journal of Physics: Conference Series*, vol. 854, 2017.

[46] J. N. Sørensen, "Aerodynamic Analysis of Wind Turbines," in *Comprehensive Renewable Energy*, Oxford, Elsevier, 2012, pp. 172-193.

[47] S. Kang, X. Yang and F. Sotiropoulos, "On the onset of wake meandering for an axial flow turbine in a turbulent open channel flow," *Journal of Fluid Mechanics*, vol. 744, pp. 376-403, 2014.

[48] T. Javaherchi, S. Antheaume and A. Aliseda, "Hierarchical Methodology for the Numerical Simulation of the Flow Field around and in the Wake of Horizontal Axis Wind Turbines: Rotating Reference Frame, Blade Element Method and Actuator Disk Model," *Wind Engineering*, vol. 38, no. 2, pp. 181-201, 2014.

[49] P. A. S. F. Silva, P. Tsoutsanis and A. F. Antoniadis, "Simple multiple reference frame for high-order solution of hovering rotors with and without ground effect," *Aerospace Science and Technology*, vol. 111, 2021.

[50] R. Franzke, S. Sebben, T. Bark, E. Willeson and A. Broniewicz, "Evaluation of the Multiple Reference FrameApproach for the Modelling of an Axial Cooling Fan," *Energies*, vol. 12, no. 15, p. 2934, 2019.

[51] L. Menegozzo, A. Dal Monte, E. Benini and A. Benato, "Small wind turbines: A numerical study for aerodynamic performance assessment under gust conditions," *Renewable Energy,* vol. 121, pp. 123-132, 2018.

[52] M. Moshfeghi, S. Shams and N. Hur, "Aerodynamic performance enhancement analysis of horizontal axis wind turbines using a passive flow control method via split blade," *Journal of Wind Engineering and Industrial Aerodynamics,* vol. 167, pp. 148-159, 2017.

[53] S. Lain, M. Garcia, B. Quintero and S. Orrego, "CFD Numerical simulations of Francis turbines," *Revista Facultad de Ingeniería Universidad de Antioquia,* vol. 51, pp. 24-33, 2010.

[54] J. Liu, H. Lin and S. R. Purimitla, "Wake field studies of tidal current turbines with different numerical methods," *Ocean Engineering,* vol. 117, pp. 383-397, 2016.

[55] C. Yang and Z. S. Mao, "Multiphase stirred reactors," in *Numerical Simulation of Multiphase Reactors with Continuous Liquid Phase*, London, Elsevier, 2014, pp. 75-151.

[56] J. Mcnaughton, S. Rolfo, I. Afgan and T. Stallard, "A simple sliding-mesh interface procedure and its application to the CFD simulation of a tidal-stream turbine," *International Journal for Numerical Methods in Fluids,* vol. 74, no. 4, pp. 250-269, 2014.

[57] K. Ng, N. J. Fentiman, K. C. Lee and M. Yianneskis, "Assessment of Sliding Mesh CFD Predictions and LDA Measurements of the Flow in a Tank Stirred by a Rushton Impeller," *Chemical Engineering Research & Design,* vol. 76, pp. 737-747, 1998.

[58] S. Yadav, S. V. Veeravalli and S. N. Singh, "COMPARISON OF PREDICTED PERFORMANCE OF VERTICAL AXIS WIND TURBINE USING OVERSET MESH AND SLIDING MESH," in *International Conference on Applied Energy*, Västerås, 2019.

[59] N. Durrani, H. Hameed, H. Rahman and S. R. Chaudhry, "A detailed Aerodynamic Design and analysis of a 2D vertical axis wind turbine using sliding mesh in CFD," in *49th AIAA Aerospace Sciences Meeting including the New Horizons Forum and Aerospace Exposition*, Orlando, 2011.

[60] N. Tonello, Y. Eude, B. de Laage de Meux and M. Ferrand, "Frozen Rotor and Sliding Mesh Models Applied to the 3D Simulation of the Francis-99 Tokke Turbine with Code_Saturne," in *Journal of Physics: Conference Series*, Lulea, 2017.

[61] P. A. S. F. Silva, T. F. de Oliveira, A. C. P. Brasil Junior and J. R. P. Vaz, "Numerical Study of Wake Characteristics in a Horizontal-Axis Hydrokinetic Turbine," *Anais da Academia Brasileira de Ciências,* vol. 88, no. 4, pp. 2441-2456, 2016.

[62] J. Jonkman, S. Butterfield, W. Musial and G. Scott, "Definition of a 5mw reference wind tturbine for offshore system development., NationalRenewable Energy Laboratory," NREL, Golden, 2009.

[63] M. Tabib, M. Salman Siddiqui, A. Rasheed and T. Kvamsdal, "Industrial scale turbine and associated wake development - comparison of RANS based Actuator Line Vs Sliding Mesh Interface Vs Multiple Reference Flame method," in *14th Deep Sea Offshore Wind R&D Conference*, Trondheim, 2017.

[64] C. Hill, V. S. Neary, B. Gunawan, M. Guala and F. Sotiropoulos, "U.S. Deparment of Energy Reference Model Program RM1: Experimental Results," Sandia National Laboratories, Minneapolis, 2014.

[65] A. Rezaeiha, I. Kalkman and B. Blocken, "Towards accurate CFD simulations of vertical axis wind turbines at different tip speed ratios and solidities: Guidelines for azimuthal increment, domain size and convergence," *Energy Conversion and Management,* vol. 156, pp. 301-316, 2018.

[66] A. Rezaeiha, I. Kalkman and B. Blocken, "CFD simulation of a vertical axis wind turbine operating at a moderate tip speed ratio: Guidelines for minimum domain size and azimuthal increment," *Renewable Energy,* vol. 107, pp. 373-385, 2017.

[67] J. Franke, "Recommendations of the COST action C14 on the use of CFD in predicting pedestrian wind environment," in *The Fourth International Symposium on Computational Wind Engineering*, Yokohama, 2006.

[68] T. Kono, S. Nebucho, T. Kogaki, T. Kiwata, S. Kimura and N. Komatsu, "Numerical Analysis of the Effects of Rotating Wind Turbine Blades on the Aerodynamic Forces Acting on Tower," *Energies,* vol. 10, no. 1, p. 121, 2017.

[69] J. Durkacz, S. Islam, R. Chan, E. Fong, H. Gillies, A. Karnik and T. Mullan, "CFD modelling and prototype testing of a Vertical Axis Wind Turbines in planetary cluster formation," *Energy Reports,* vol. 7, pp. 119-126, 2021.

[70] H. D. Nedjari, O. Guerri and M. Saighi, "CFD wind turbines wake assessment in complex topography," *Energy Conversion and Management,* vol. 138, pp. 224-236, 2017.

[71] M. E. Harrison, W. M. J. Batten, L. E. Myers and A. S. Bahaj, "Comparison between CFD simulations and experiments for predicting the far wake of horizontal axis tidal turbines," *IET Renewable Power Generation,* vol. 4, no. 6, pp. 613-627, 2010.

[72] V. Neary, B. Gunawan, C. Hill and L. P. Chamorro, "Near and far field flow disturbances induced by model hydrokinetic turbine: ADV and ADP comparison," *Renewable Energy,* vol. 60, pp. 1-6, 2013.

[73] R. Whittlesey, "Vertical Axis Wind Turbines: Farm and Turbine Design," in *Wind Energy Engineering,* Academic Press, 2017, pp. 185-202.

[74] B. Gunawan, V. S. Neary, J. Mortensen and J. D. Roberts, "Assessing and Testing Hydrokinetic Turbine Performance and Effects on Open Channel Hydrodynamics: An Irrigation Canal Case Study," Sandia National Laboratories, 2017.

[75] I. Bostan, V. Dulgheru, I. Sobor, V. Bostan and A. Sochireanu, "DEVELOPMENT, MANUFACTURE AND TESTING OF HORIZONTAL AXIS WIND MICROTURBINES WITH POWER OF 10 KW," *Annals of the University of Craiova, Electrical Engineering Series,* vol. 35, pp. 71-76, 2011.

[76] M. Sood and S. K. Singal, "Development of hydrokinetic energy technology: A review," *International Journal of Energy Research,* vol. 43, no. 11, pp. 5552-5571, 2019.

[77] P. K. Modali, A. Vinod and A. Banerjee, "Towards a better understanding of yawed turbine wake for efficient wake steering in tidal arrays," *Renewable Energy,* vol. 177, pp. 482-494, 2021.

[78] M. J. Govea, J. H. VanZwieten, A. Mink, G. Alsenas, F. Dalgleish and Y. Tang, "Motion compensation of opean-ocean acoustic Doppler velocimeter

measurements for offshore turbulence assessment," in *Oceans 2022*, Hampton Roads, 2022.

[79] W. Deng, Z. Li, L. Ji, L. Shang, D. Liu and X. Liu, "Laser Doppler Velocimetry Test of Flow Characteristics in Draft Tube of Model Pump Turbine," *Processes,* vol. 10, no. 7, 2022.

[80] M. Slama, G. Pinon, C. El Hadi, M. Togneri, B. Gaurier, G. Germain, J. V. Facq, J. Nuno, P. Mansilla, E. Nicolas, J. Marcille and A. Pacheco, "Turbine design dependency to turbulence: Anexperimental study of three scaled tidal turbines," *Ocean Engineering,* vol. 234, 2021.

[81] W. Deng, L. Xu, Z. Li, W. Tang, X. Wang, L. Shang, D. Liu and X. Liu, "Stability Analysis of Vaneless Space in High-Head Pump-Turbine under Turbine Mode: Computational Fluid Dynamics Simulation and Particle Imaging Velocimetry Measurement," *Machines,* vol. 10, no. 2, 2022.

[82] D. Duda, T. Jelinek, P. Milcak, M. Nemec, V. Uruba, V. Yanovych and P. Zitek, "Experimental Investigation of the Unsteady Stator/Rotor Wake Characteristics Downstream of an Axial Air Turbine," *International Journal of Turbomachinery Propulsion and Power,* vol. 6, no. 3, 2021.

[83] F. Attene, F. Balduzzi, A. Bianchini and M. S. Campobasso, "Using Experimentally Validated Navier-Stokes CFD to Minimize Tidal Stream Turbine Power Losses Due to Wake/Turbine Interactions," *Sustainability,* vol. 12, no. 21, 2020.

[84] A. Rezaeiha and D. Micallef, "Wake interactions of two tandem floating offshore wind turbines: CFD analysis using actuator disc model," *Renewable Energy,* vol. 179, pp. 859-876, 2021.

[85] T. Castiglione, S. Barbarelli, G. Lo Zupone and S. Bova, "Flow-field and wake analysis of novel double-rotor open-center tidal current turbine by CFD simulations," *Ocean Engineering,* vol. 222, 2021.

[86] S. Badshah, M. Badshah, N. Hafeez, S. Jan and Z. U. Rehman, "CFD Analysis of Tidal Current Turbine Performance with Different Boundary Conditions," *IOP Conference Series: Earth and Environmental Science,* vol. 581, 2020.

[87] J. Cousteix, "Aircraft Aerodynamic Boundary Layers," in *Encyclopedia of Physical Science and Technology*, Third ed., Academic Press, 2003, pp. 301-317.

[88] C. Garrett and P. Cummins, "The Efficiency of a Turbine in a Tidal Channel," *Journal of Fluid Mechanics,* vol. 588, pp. 243-251, 2007.

[89] C. Garrett and P. Cummins, "The Power Potential of Tidal Currents in Channels," *Proceedings of the Royal Society A,* vol. 461, pp. 2563-2572, 2005.

[90] T. Nishino and R. H. J. Willden, *Journal of Fluid Mechanics,* vol. 708, pp. 596-606, 2012.

[91] T. Divett, "Optimising design of large tidal energy arrays in channels: layout and turbine tuning for maximum power capture using large eddy simulations with adaptive mesh," [Doctoral dissertation, University of Otago], https://ourarchive.otago.ac.nz/handle/10523/4995, 2014.

[92] A. Benavides-Moran, L. Rodriguez-Jaime and S. Lain, "Numerical Investigation of the Performance, Hydrodynamics, and Free-Surface Effects in Unsteady Flow of a Horizontal Axis Hydrokinetic Turbines," *Processes,* vol. 10, p. 69, 2021.